NASA/TP-1999-209540

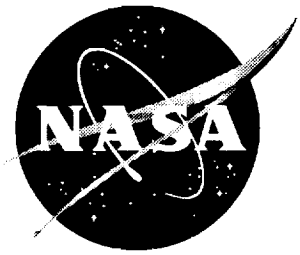

Turbulence Model Comparisons for a High-Speed Aircraft

Melissa B. Rivers and Richard A. Wahls
Langley Research Center, Hampton, Virginia

December 1999

The NASA STI Program Office . . . in Profile

Since its founding, NASA has been dedicated to the advancement of aeronautics and space science. The NASA Scientific and Technical Information (STI) Program Office plays a key part in helping NASA maintain this important role.

The NASA STI Program Office is operated by Langley Research Center, the lead center for NASA's scientific and technical information. The NASA STI Program Office provides access to the NASA STI Database, the largest collection of aeronautical and space science STI in the world. The Program Office is also NASA's institutional mechanism for disseminating the results of its research and development activities. These results are published by NASA in the NASA STI Report Series, which includes the following report types:

- TECHNICAL PUBLICATION. Reports of completed research or a major significant phase of research that present the results of NASA programs and include extensive data or theoretical analysis. Includes compilations of significant scientific and technical data and information deemed to be of continuing reference value. NASA counterpart of peer-reviewed formal professional papers, but having less stringent limitations on manuscript length and extent of graphic presentations.

- TECHNICAL MEMORANDUM. Scientific and technical findings that are preliminary or of specialized interest, e.g., quick release reports, working papers, and bibliographies that contain minimal annotation. Does not contain extensive analysis.

- CONTRACTOR REPORT. Scientific and technical findings by NASA-sponsored contractors and grantees.

- CONFERENCE PUBLICATION. Collected papers from scientific and technical conferences, symposia, seminars, or other meetings sponsored or co-sponsored by NASA.

- SPECIAL PUBLICATION. Scientific, technical, or historical information from NASA programs, projects, and missions, often concerned with subjects having substantial public interest.

- TECHNICAL TRANSLATION. English-language translations of foreign scientific and technical material pertinent to NASA's mission.

Specialized services that complement the STI Program Office's diverse offerings include creating custom thesauri, building customized databases, organizing and publishing research results . . . even providing videos.

For more information about the NASA STI Program Office, see the following:

- Access the NASA STI Program Home Page at ***http://www.sti.nasa.gov***

- Email your question via the Internet to help@sti.nasa.gov

- Fax your question to the NASA STI Help Desk at (301) 621-0134

- Telephone the NASA STI Help Desk at (301) 621-0390

- Write to:
  NASA STI Help Desk
  NASA Center for AeroSpace Information
  7121 Standard Drive
  Hanover, MD 21076-1320

NASA/TP-1999-209540

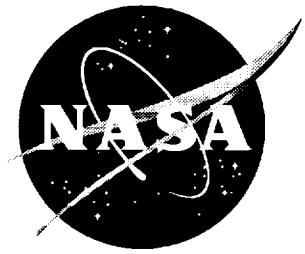

Turbulence Model Comparisons for a High-Speed Aircraft

Melissa B. Rivers and Richard A. Wahls
Langley Research Center, Hampton, Virginia

National Aeronautics and
Space Administration

Langley Research Center
Hampton, Virginia 23681-2199

December 1999

The use of trademarks or names of manufacturers in this report is for accurate reporting and does not constitute an official endorsement, either expressed or implied, of such products or manufacturers by the National Aeronautics and Space Administration.

Available from:

NASA Center for AeroSpace Information (CASI)
7121 Standard Drive
Hanover, MD 21076-1320
(301) 621-0390

National Technical Information Service (NTIS)
5285 Port Royal Road
Springfield, VA 22161-2171
(703) 605-6000

Summary

Four turbulence models are described and evaluated for transonic flows over the High-Speed Research/ industry baseline configuration known as Reference H by using the thin-layer, upwind, Navier-Stokes solver known as CFL3D. The turbulence models studied are the equilibrium model of Baldwin-Lomax (B-L) with the Degani-Schiff (D-S) modifications, the one-equation Baldwin-Barth (B-B) model, the one-equation Spalart-Allmaras (S-A) model, and Menter's two-equation Shear Stress Transport (SST) model. The flow conditions, which correspond to tests performed in the National Transonic Facility (NTF) at Langley Research Center, are a Mach number of 0.90 and a Reynolds number of 30×10^6 based on mean aerodynamic chord for angles of attack of 1°, 5°, and 10°. The effects of grid topology and the representation of the actual wind tunnel model geometry are also investigated. Computed forces and surface pressures compare reasonably well with the experimental data for all four turbulence models.

Introduction

Increasing computer capacity and the development of efficient numerical methods allow the solution of the Navier-Stokes equations for practical aerodynamic applications such as a next generation supersonic transport. Of crucial importance for the accuracy of the results is the performance of the turbulence model because the viability of a supersonic transport is, in part, based upon the ability to predict drag to within one count. It has been observed during the High-Speed Research (HSR) program that computational solutions have been inconsistent, showing dependence on turbulence model and model orientation, among other factors (ref. 1). With the increasing complexity of the flows under investigation, the demand for reliable turbulence models is as high as ever; these models must perform well for attached flow and at least the onset of separated flow that occurs over an angle-of-attack range. The search for a new or improved turbulence model that accurately predicts both attached and separated three-dimensional flow fields is complicated by inherent limitations in the computational fluid dynamics (CFD) codes such as truncation error, grid density, the type of differencing scheme employed, and for central-difference schemes, the amount of artificial dissipation added for numerical stability.

This paper investigates the ability of four different turbulence models to predict accurately the transonic flow over the High-Speed Research/industry baseline configuration known as Reference H. This configuration is an attached flow airplane that goes to separated flow at high angles of attack. The thin-layer Navier-Stokes solver CFL3D (ref. 2) was run using the Spalart-Allmaras (S-A) (ref. 3), the Baldwin-Lomax (B-L) (ref. 4) with the Degani-Schiff (D-S) modifications (ref. 5), the Baldwin-Barth (B-B) (ref. 6), and Menter's Shear Stress Transport (SST) turbulence models (ref. 7) for this study. Each model is discussed in detail herein. No attempt was made to tune these turbulence models for this configuration.

Symbols

$a_{1(\mathrm{SST})}$	constant used in Menter's Shear Stress Transport turbulence model
b	model span, in.
C_D	drag coefficient
C_{Dp}	pressure component of drag coefficient
C_{Dv}	viscous component of drag coefficient
C_L	lift coefficient
C_m	pitching-moment coefficient
C_p	pressure coefficient
$\bar{c}$	mean aerodynamic chord, in.

c	local chord, in.
D	function in Baldwin-Lomax turbulence model
$d_{(\text{S-A})}$	distance closest to any wall in Spalart-Allmaras turbulence model, in.
e	total energy per unit volume, ft-lb/ft^3
F	function in Baldwin-Lomax turbulence model
F, G, H	inviscid fluxes
$F_{1_{(\text{SST})}}, F_{2_{(\text{SST})}}$	functions used in Menter's Shear Stress Transport turbulence model
$F_{2_{(\text{B-B})}}, F_{3_{(\text{B-B})}}, D_{1_{(\text{B-B})}}, D_{2_{(\text{B-B})}}$	viscous sublayer damping terms used in Baldwin-Barth turbulence model
$f_{t2_{(\text{S-A})}}, f_{v2_{(\text{S-A})}}, f_{\omega_{(\text{S-A})}}$	functions in Spalart-Allmaras turbulence model
F_v, G_v, H_v	viscous fluxes
$\mathbf{J}$	Jacobian matrix
k	kinetic energy, slug-ft^2/sec^2
L/D	lift-to-drag ratio
M	free-stream Mach number
$P_{(\text{B-B})}$	production term used in Baldwin-Barth turbulence model
Q	conservation variables
q	dynamic pressure, psf
$\text{Re}_{\bar{c}}$	Reynolds number based on mean aerodynamic chord
Re_T	turbulence Reynolds number
$\text{R}\tilde{\text{e}}_{T_{(\text{B-B})}}$	working variable related to Re_T, $\text{Re}_T = (\text{R}\tilde{\text{e}}_{T_{(\text{B-B})}}) f_{3_{(\text{B-B})}}(\text{R}\tilde{\text{e}}_{T_{(\text{B-B})}})$ in Baldwin-Barth turbulence model
t	time, sec
u, v, w	Cartesian velocities in x, y, and z directions, respectively, ft/sec
$\mathbf{u}_{i_{(\text{SST})}}$	velocity vector used in Menter's Shear Stress Transport turbulence model, ft/sec
x, y, z	Cartesian coordinates, in.
$\mathbf{x}_{j(\text{SST})}$	position vector used in Menter's Shear Stress Transport turbulence model, in.
y	distance to wall or wake cut in Baldwin-Lomax turbulence model
y^+	law-of-the-wall coordinate, $\frac{y\sqrt{\rho\tau_w}}{\mu}$
α	angle of attack, deg
$\beta_{(\text{SST})}, \beta^*_{(\text{SST})}$	constants used in Menter's Shear Stress Transport turbulence model
Γ	Klebanoff intermittency factor used in Baldwin-Lomax turbulence model
$\gamma_{(\text{SST})}$	constant used in Menter's Shear Stress Transport turbulence model

μ	molecular viscosity, slugs/ft-sec
μ_t	molecular eddy viscosity, slugs/ft-sec
μ_w	molecular viscosity at wall in Baldwin-Lomax turbulence model, slugs/ft-sec
ν	kinematic viscosity, ft^2/sec
$\tilde{\nu}_{(S\text{-}A)}$	working variable in Spalart-Allmaras turbulence model
ν_t	kinematic eddy viscosity, ft^2/sec
ξ, η, ζ	general curvilinear coordinates
ρ	density, $slugs/ft^3$
ρ_w	density at the wall in Baldwin-Lomax turbulence model, $slugs/ft^3$
$\sigma_{\varepsilon(B\text{-}B)}$	function used in Baldwin-Barth turbulence model
$\sigma_{k(SST)}$, $\sigma_{\omega(SST)}\sigma_{\omega 2(SST)}$	constants used in Menter's Shear Stress Transport turbulence model
$\tau_{ij(SST)}$	Reynolds stress tensor used in Menter's Shear Stress Transport turbulence model
τ_w	local shear stress in Baldwin-Lomax turbulence model, lb/in^2
Ω	magnitude of vorticity, $\sqrt{\left(\frac{\partial u}{\partial y}-\frac{\partial v}{\partial x}\right)^2+\left(\frac{\partial v}{\partial z}-\frac{\partial w}{\partial y}\right)^2+\left(\frac{\partial w}{\partial x}-\frac{\partial u}{\partial z}\right)^2}$
ω	specific dissipation rate, 1/sec

Abbreviations:

AF	approximate factorization
B-B	Baldwin-Barth
B-L	Baldwin-Lomax with Degani-Schiff modifications
C-O	C in streamwise direction; O in spanwise direction
CPU	central processing unit
D-S	Degani-Schiff
Exp.	experiment
FAS	full-approximation scheme
HSR	high-speed research
LE	leading edge
MW	megawords
NAS	Numerical Aerospace Simulator
O-C	O in streamwise direction; C in spanwise direction
PDE	partial differential equation
resid	residual
S-A	Spalart-Allmaras
SST	Shear Stress Transport

Subscripts:

i	inner region values
ij	tensor notation indices
max	maximum value
min	minimum value
o	outer region values
t	differentiation in time
x, y	differentiation in x and y directions, respectively
w	conditions at wall
wake	conditions in wake

Experimental Study

Tests of the High-Speed Research/industry baseline configuration known as Reference H have been conducted in the National Transonic Facility (NTF) at Langley Research Center. The 2.2-percent scale model of the clean wing-body configuration is shown in the NTF test section in figure 1; the model has a wing span of 34.23 in., a mean aerodynamic chord ($\bar{c}$) of 22.71 in., a reference area of 3.436 ft^2, and pitching-moment data have been referenced to the 50-percent $\bar{c}$ location ($x = 46.445$ in.). The leading-edge sweep of the wing is 76° inboard of the 23-percent semispan, 68.5° from the 23-percent to the 52-percent semispan, and 48° outboard of the 52-percent semispan. The leading edge is blunt inboard of the 52-percent semispan and sharp outboard of the 52-percent semispan. Figure 2 shows the location of the six spanwise pressure rows on the wing, and figure 3 shows the location of the three chordwise pressure rows on the wing of this geometry. Although the shaded area in these two figures was part of the metric model in the wind tunnel experiment, it was not part of the computational model in order to make the grid generation easier.

The NTF is a cryogenic, pressure wind tunnel with independent control of pressure, temperature, and fan speed. The independent controls allow Mach number, Reynolds number, and dynamic pressure to be varied independently. Flow conditions used for comparison herein are a Mach number of 0.90, a Reynolds number based on the mean aerodynamic chord of 30×10^6, and a dynamic pressure of 1005 psf. The variable dynamic pressure enables an extrapolation of the data to a constant dynamic pressure, which eliminates the effects of static aeroelastic model deformation from the wind tunnel data. In addition, the dynamic pressure step is required to connect low Reynolds number data to high Reynolds number data (10×10^6 to 80×10^6) due to facility limitations which prohibit the full Reynolds number sweep to be performed at a constant dynamic pressure.

Data presented were acquired in two separate tests: the first test acquired surface pressure data, and the second test acquired force-and-moment data without the potentially adverse influence of pressure instrumentation on the balance. Uncertainty of the pressure coefficients was estimated to be less than ±0.01 at a 95-percent confidence level. The observed variability in the lift, drag, and pitching-moment coefficients was ±0.003, ±0.0003, and ±0.0005, respectively.

Computational Method

Computational Algorithm

The computational method used in this study is version 4 of the CFL3D Navier-Stokes code described in detail in reference 2. This code, developed at Langley Research Center, solves the three-dimensional

time-dependent thin-layer Navier-Stokes equations with a finite-volume formulation. The equations are written in conservation form with the generalized curvilinear coordinates ξ, η, and ζ as

$$\frac{\partial Q}{\partial t} + \frac{\partial F}{\partial \xi} + \frac{\partial G}{\partial \eta} + \frac{\partial}{\partial \zeta}(H - H_V) = 0 \tag{1}$$

where

$$Q = \frac{1}{J}[\rho \ \rho u \ \rho v \ \rho w \ e] \tag{2}$$

The coordinates ξ, η, and ζ are oriented essentially in the streamwise, spanwise, and normal directions, respectively. It is assumed that the ζ coordinate lines are nearly orthogonal to the body at the body surface. The symbols t, ρ, u, v, w, and e denote the time, density, Cartesian velocity components, and total energy per unit volume, respectively; F, G, and H are the inviscid fluxes in the ξ, η, and ζ directions, respectively; and H_v is the viscous flux in the ζ direction. The viscous fluxes, F_v and G_v, are dropped from the governing equations because of the thin-layer assumption, in which the dominant effects are assumed to arise from the viscous diffusion normal to the body surface. The state equations are written assuming an ideal gas. Molecular viscosity is calculated by using Sutherland's law and Stoke's hypothesis. The Reynolds stresses are modeled using the four turbulence models described in the Turbulence Models section. The governing equations are discretized to be consistent with conservation laws in integral form.

A second-order accurate upwind-biased spatial differencing scheme is used for solving these equations. Roe's flux-difference splitting (ref. 8) is used to construct the upwind differences for the convective and the pressure terms. The spatial derivatives are written conservatively as a flux balance across the cell, and the shear stress and heat transfer terms are centrally differenced. Spatial approximate factorization (AF) and Euler backward integration after linearization in time results in the solution through 5 by 5 block-tridiagonal matrix inversions in three directions. An approximate diagonal form of the spatial factors is employed to reduce computational time. Convergence acceleration is obtained by using a multigrid full-approximation scheme (FAS) and mesh sequencing for flow initialization.

Turbulence Models

Baldwin-Lomax with Degani-Schiff modification. The Baldwin-Lomax turbulence model (ref. 4) is used widely throughout the CFD community; its capabilities and limitations are well-known. In short, it is generally considered a good model for the prediction of attached flows, but it is deficient for flows with any significant separated regions. In particular, the Baldwin-Lomax model tends to predict shocks too far downstream for separated transonic flows over aerodynamic configurations. Degani and Schiff (ref. 5) modified the original Baldwin-Lomax model to extend the model in a rational manner to permit an accurate determination of the viscous length scale for high-angle-of-attack flows in regions of cross-flow separation in which a strong leeward vortical flow structure exists.

The original Baldwin-Lomax model is a two-layer algebraic model. The inner eddy viscosity is determined via

$$\mu_{t,i} = \rho(0.4Dy)^2\Omega \tag{3}$$

where

$$D = 1 - \exp\left(\frac{-y^+}{26}\right) \tag{4}$$

and

$$y^{+}_{(\text{Baldwin-Lomax})} = \frac{y\sqrt{\rho_w \tau_{w_{(B\text{-}L)}}}}{\mu_{w_{(B\text{-}L)}}} \tag{5}$$

where y is the distance to the wall or wake cut, Ω is the magnitude of the vorticity, and the subscript w refers to a wall value.

The outer eddy viscosity is given by

$$\mu_{t,\,o} = (0.0168)(1.6)\rho F_{\text{wake}} \Gamma \tag{6}$$

where

$$F_{\text{wake}} = \min\left[y_{\max} F_{\max}, \frac{y_{\max}\left(\sqrt{u_i u_{i_{\max}}} - \sqrt{u_i u_{i_{\min}}}\right)^2}{F_{\max}} \right] \tag{7}$$

and

$$\Gamma = \frac{1}{1 + 5.5\left(\dfrac{0.3y}{y_{\max}}\right)^6} \tag{8}$$

and

$$F = y\Omega D \tag{9}$$

In wakes, D is assumed to be 1. The subscript max in equations (7) and (8) refers to the value at the location where F is at its maximum along grid lines that are oriented normal to the body (i.e., in the viscous direction for thin-layer Navier-Stokes).

The eddy viscosity μ_t is determined by marching away from the wall along these same grid lines and is taken as $\mu_{t,i}$ from the wall (where the value is zero) to the point above the wall where $\mu_{t,i}$ first exceeds $\mu_{t,o}$. Thereafter μ_t is given the value $\mu_{t,o}$. Transition is modeled by setting μ_t to zero along all grid lines that are normal to the wall within a preselected range of laminar flow.

The major difficulty encountered in applying the Baldwin-Lomax turbulence model to bodies with cross-flow separation is that of properly evaluating the scale length $y_{\max}$ and, in turn, of determining $\mu_{t,o}$ for boundary layer profiles in the cross-flow separation region. This difficulty arises because multiple points of local maximum can be obtained in vortical flow regions. To eliminate these difficulties, Degani and Schiff modified the Baldwin-Lomax turbulence model so that at each axial station the code searches radially outward along successive rays, sweeping from the windward to the leeward plane of symmetry. Along each ray, the code sweeps outward to find the first peak in $F(y)$ and cuts off the search when the peak is reached. To prevent the selection of extraneous peaks that might be caused by an unsteady behavior in $F(y)$, a peak is considered to have been found when the value of $F(y)$ drops to 90 percent of the local maximum value.

As proposed by Baldwin and Lomax, the turbulence model examines a quantity containing the local fluid vorticity magnitude to determine the length scale and thus the eddy viscosity coefficient. The modifications made by Degani and Schiff (ref. 5) permit the model to differentiate between the vorticity within the attached boundary layers from the vorticity on the surfaces of separation and thus to select a length scale

based on the thickness of the attached boundary layers rather than one based on the radial distance between the body surface and the surface of separation. The latter scale length can be much greater than that based on the boundary layer thickness, and if used, the resulting eddy-viscosity coefficient can be as much as two orders of magnitude too high. In general, the eddy-viscosity coefficient will cause the primary vortices to be smaller than those observed experimentally, and the primary separation line will be located closer to the leeward symmetry plane. In addition, the secondary (and tertiary) separation lines will not occur in the computed flows.

Baldwin-Barth. The Baldwin-Barth (B-B) turbulence model (ref. 6) is a one-equation turbulence model derived from a simplified form of the k-ε equations. The model solves a partial differential equation (PDE) over the whole field for the turbulent Reynolds number R_T, which is directly related to the kinematic eddy viscosity ν_t:

$$\frac{D\left(\nu\tilde{Re}_{T_{(B\text{-}B)}}\right)}{Dt} = \left(\nu + \frac{1.0}{\sigma_{\varepsilon_{(B\text{-}B)}}}\nu_t\right)\nabla^2\left(\nu\tilde{Re}_{T_{(B\text{-}B)}}\right) - \frac{1.0}{\sigma_{\varepsilon_{(B\text{-}B)}}}(\nabla\nu_t)\cdot\nabla\left(\nu\tilde{Re}_{T_{(B\text{-}B)}}\right) + \left(2f_{2_{(B\text{-}B)}} - 1.2\right)\sqrt{\nu\tilde{Re}_{T_{(B\text{-}B)}}P_{(B\text{-}B)}} \tag{10}$$

Then

$$\mu_t = 0.09\rho\left(\nu\tilde{Re}_{T_{(B\text{-}B)}}\right)D_{1_{(B\text{-}B)}}D_{2_{(B\text{-}B)}} \tag{11}$$

The variables ν_t, $\sigma_{\varepsilon_{(B\text{-}B)}}$, $f_{2_{(B\text{-}B)}}$, $P_{(B\text{-}B)}$, $D_{1_{(B\text{-}B)}}$, and $D_{2_{(B\text{-}B)}}$ are described in detail in reference 6. In this formulation of the B-B turbulence model, the thin-layer assumption has been used for the source term (the last term in the PDE).

This equation is solved implicitly by using 3-factor AF, with first-order upwind differencing used on the advective terms. Local time stepping is employed to accelerate convergence. The transition location is modeled by phasing out the source term along all grid lines that are normal to the wall within a preselected range of laminar flow.

Spalart-Allmaras. The Spalart-Allmaras (S-A) turbulence model is a one-equation turbulence model derived by "using empiricism and arguments of dimensional analysis, Galilean invariance, and selective dependence on the molecular viscosity" (ref. 3). The model solves a PDE over the whole field for a working variable $\tilde{\nu}_{(S\text{-}A)}$ related to the eddy viscosity:

$$\frac{D\tilde{\nu}_{(S\text{-}A)}}{Dt} = -0.933\tilde{\nu}_{(S\text{-}A)}\nabla^2\tilde{\nu}_{(S\text{-}A)} + 1.5\nabla\cdot[(\nu + 1.622\tilde{\nu}_{(S\text{-}A)})\nabla\tilde{\nu}_{(S\text{-}A)}] + 0.1355\left(1 - f_{t2_{(S\text{-}A)}}\right)\Omega\tilde{\nu}_{(S\text{-}A)} + \left\{0.8061\left[\left(1 - f_{t2_{(S\text{-}A)}}\right)f_{\nu2_{(S\text{-}A)}} + f_{t2_{(S\text{-}A)}}\right] - 3.2391 f_{w_{(S\text{-}A)}}\right\}\left(\frac{\tilde{\nu}_{S\text{-}A}}{d_{S\text{-}A}}\right)^2 \tag{12}$$

Then

$$\mu_t = \frac{\rho\tilde{\nu}_{(S\text{-}A)}(\tilde{\nu}_{(S\text{-}A)}/\nu)^3}{(\tilde{\nu}_{(S\text{-}A)}/\nu)^3 + 357.911} \tag{13}$$

The terms $f_{t2_{(S\text{-}A)}}$, $f_{v2_{(S\text{-}A)}}$, and $f_{w_{(S\text{-}A)}}$ are described in detail in reference 3. The term $d_{(S\text{-}A)}$ denotes the nearest distance to any wall. The S-A model is very similar in form to the B-B model, although the S-A model includes a destruction term that is not present in the other model. This lack of a destruction term in the B-B model is responsible for a mild inconsistency in modeling isotropic turbulence and could also invalidate the model in the class of shear flows in which ν_t decreases (such as an axisymmetric wake). The PDE is solved with the same implicit method used in the B-B model, and transition is modeled in a similar fashion as well.

Menter's SST. The Menter's Shear Stress Transport (SST) turbulence model is a modified version of the k-ω two-equation turbulence model. This model is based on Bradshaw's assumption that the principal shear-stress is proportional to the turbulent kinetic energy, which is introduced into the definition of the eddy viscosity. This model transforms a k-ε model into a k-ω formulation, and then the original equation is multiplied by a function $F_{1(SST)}$, and the transformed model is multiplied by a function (1-F). Both are added together, giving the following equations:

$$\frac{D\rho k}{Dt} = \tau_{ij_{(SST)}}\frac{\partial u_{i_{(SST)}}}{\partial x_{j_{(SST)}}} - \beta^*_{(SST)}\rho\omega k + \frac{\partial}{\partial x_{j_{(SST)}}}\left[(\mu + \sigma_{k_{(SST)}}\mu_t)\frac{\partial k}{\partial x_{j_{(SST)}}}\right] \tag{14}$$

$$\frac{D\rho\omega}{Dt} = \frac{\gamma_{(SST)}}{\nu_t}\tau_{ij_{(SST)}}\frac{\partial u_{i_{(SST)}}}{\partial x_{j_{(SST)}}} - \beta_{(SST)}\rho\omega^2 + \frac{\partial}{\partial x_{j_{(SST)}}}\left[(\mu + \sigma_{\omega_{(SST)}}\mu_t)\frac{\partial\omega}{\partial x_{j_{(SST)}}}\right]$$
$$+ 2(1-F_1)\rho\sigma_{\omega 2_{(SST)}}\frac{1}{\omega}\frac{\partial k}{\partial x_{j_{(SST)}}}\frac{\partial\omega}{\partial x_{j_{(SST)}}} \tag{15}$$

where the constants $\beta^*_{(SST)}$, $\gamma_{(SST)}$, $\sigma k_{(SST)}$, $\sigma\omega_{(SST)}$, $\beta_{(SST)}$, and $F_{1_{(SST)}}$ are described in detail in reference 7. The eddy viscosity is defined as

$$\mu_t = \frac{\rho a_{1_{(SST)}} k}{\max\left(a_{1_{(SST)}}\omega; \Omega F_{2_{(SST)}}\right)} \tag{16}$$

where Ω is the magnitude of the vorticity; $F_{2(SST)}$ and $a_{1(SST)}$ are also described in detail in reference 7.

Grid Generation

The grid generated about the NTF 2.2-percent HSR Reference H baseline geometry (fig. 1) was created using the GRIDGEN grid generation package (ref. 9). Three grids were generated for this geometry in order to assess the effect of grid topology and the representation of the actual wind tunnel model geometry. The different topologies and geometric representations were chosen because these topologies and geometric representations are the most common ones used for this configuration.

The first grid was a two-block grid with an O-C (O in the streamwise direction and C in the spanwise direction) topology with a 5-in. full-scale transition from blunt-to-sharp leading edge at the crank location on the wing (fig. 4). This grid had 105 points in the streamwise direction, 177 points in the spanwise direction, and 81 points normal to the surface in the first block, which defines the wing-body configuration; the second block, which defines the sting, had 49 points in the streamwise direction, 177 points in the spanwise direction, and 81 points normal to the surface. The total number of grid points was 2207898. The normal spacing adjacent to the surface was 5×10^{-5} over the entire surface. The surface spacing distribution corresponds to a nondimensional y^+ value of approximately 1.6 for $M = 0.90$ and $\mathrm{Re}_{\bar{c}} = 30 \times 10^6$. The far-field boundary extends to $20\bar{c}$ in the circumferential and upstream directions, and the second block extends approximately $20\bar{c}$ downstream of the first block.

The second grid used was a single block C-O (C in the streamwise direction and O in the spanwise direction) topology grid with a 5-in. full-scale transition from blunt-to-sharp wing leading edge at the crank; this grid defines both the wing-body configuration and the sting. This grid had 133 points in the spanwise direction, 249 points in the streamwise direction, and 81 points in the normal direction. The total number of grid points was 2682477. The normal spacing was 5×10^{-5} over the entire surface. The surface spacing distribution corresponds to a nondimensional y^+ value of approximately 1.0 for $M = 0.90$ and $\mathrm{Re}_{\bar{c}} = 30 \times 10^{-6}$. The far-field boundary extends to $20\bar{c}$ in the circumferential, upstream, and downstream (of the wing-body configuration) directions. Figure 4 shows the differences in the surface grids of the O-C grid on the wing with a 5-in. full-scale transition from blunt-to-sharp wing leading edge and the C-O grid on the wing with a 5-in. full-scale transition from blunt-to-sharp wing leading edge. Figure 5 shows a representation of the volume grid for the C-O grid topology with a 1-in. full-scale transition from blunt-to-sharp wing leading edge. Figures 6 and 7 show that both grids are converged for lift and that the C-O grid is converged for drag at the given conditions. The poor convergence quality of the O-C grid is believed to be caused by a lack in the grid quality. The results presented in this paper are for the finest mesh, and the differences due to the mesh topology will be discussed in the Results and Discussion section.

The wind tunnel model had a discontinuity between the sharp wing leading edge and the blunt wing leading edge at the crank. In an attempt to model this discontinuity, a third grid was generated that was identical to the second grid (C-O topology) with the exception of a 1-in., rather than a 5-in., full-scale geometric transition region between the blunt and sharp wing leading edges at the crank. Figure 8 shows the differences in the surface grids of the C-O grid on the wing with a 5-in. full-scale transition from blunt-to-sharp wing leading edge and the C-O grid on the wing with a 1-in. full-scale transition from blunt-to-sharp wing leading edge. The sketch shows where the geometric wedge is on the wing and what is meant by a 1-in. versus a 5-in. full-scale geometric transition from blunt-to-sharp wing leading edge.

Results and Discussion

Grid Topology and Wedge Size

A grid study was performed with the three grids described previously to determine which grid gave the best comparisons with the experimental data. All runs made for this grid study were performed at $M = 0.90$, $\mathrm{Re}_{\bar{c}} = 30 \times 10^6$, and at $\alpha = 5°$. These runs were all made with CFL3D by using the S-A turbulence model. Figure 9 shows the pressure distributions at the six spanwise stations on the wing of the HSR 2.2-percent NTF geometry for the C-O topology, the O-C topology, and the experimental data. Figure 10 shows the pressure contours for the two topologies. As shown in figure 9, both topologies show similar agreement with the experimental data, except aft of the crank of the wing ($x = 46.5$ in.) where the C-O topology picks up more of the characteristics of the experimental pressure distribution than does the O-C topology. The pressure contours in figure 10 show that the C-O grid topology yields a different surface pressure distribution than the O-C grid topology, primarily on the outboard wing panel.

Figure 11 shows the pressure distributions at the six spanwise stations on the wing of the HSR 2.2-percent NTF geometry for the 1-in. full-scale wedge versus the 5-in. full-scale wedge. Figure 12 shows the pressure contours of the two wedge sizes. As shown in figures 11 and 12, the wedge size does not have a significant effect on the pressure distributions or the pressure contours. After we looked at the results from these two studies, the single block C-O grid with the 1-in. wedge was used for the turbulence model study because the 1-in. wedge more closely represents the actual wind tunnel model geometry.

Code Modifications

During this study, the CFL3D Navier-Stokes code was modified to increase the calculation accuracy of the minimum distance function by incorporating a surface interpolation scheme based on normal projection. The prior approach used the nearest body cell center point. This modification only affected the results of the S-A and SST turbulence models. The minimum distance function affects the $f_{w_{(S\text{-}A)}}$ and $d_{(S\text{-}A)}$ terms in equation (12) for the S-A model and the $F_{1(SST)}$ term in equation (15) for the SST model. Figures 13 and 14 show that the modification made to the code does not significantly affect the pressure distributions when either the S-A turbulence model or Menter's SST turbulence model is used, respectively. Figure 15, however, indicates that the forces are affected by this modification to CFL3D. This change is seen because the modification changes the solution, which, in turn, results in a change in the integrated forces. For the S-A case, the lift is increased by approximately 0.004 and the drag is decreased by approximately 20 drag counts. For Menter's SST results, the lift remains about the same, but the drag is increased by 3 drag counts. The change to the code brought the two calculations into closer agreement with each other but took the S-A results farther away from the experimental data.

This modification also decreased the amount of computer time needed to obtain a converged solution by approximately 40 percent for the S-A case. The SST case was restarted from the previous runs with the new code, while the S-A case was completely rerun with the new code; therefore, the amount of time savings for the SST case is unknown, but it is expected to decrease the amount of computational time by about the same amount as observed with the S-A model.

Turbulence Model Comparison

Four different turbulence models, the equilibrium model of Baldwin-Lomax with the Degani-Schiff modifications, the one-equation Baldwin-Barth model, the one-equation Spalart-Allmaras model, and Menter's two-equation Shear Stress Transport model were used to perform runs for the HSR 2.2-percent NTF geometry at $M = 0.90$, $\mathrm{Re}_{\bar{c}} = 30 \times 10^6$, and at three angles of attack, 1°, 5°, and 10°. In this investigation, it is assumed that the entire boundary layer flow is turbulent. All computations were performed with CFL3D using a C-O topology grid with approximately 2.7 million grid points.

The solutions were considered to be converged when the drag coefficient changed less than one drag count over 100 iterations and when the residual was decreased by at least three orders of magnitude. Typical convergence histories for all three angles of attack are shown in figures 16 through 18; the run procedure, along with the run time, is given for the residual history for each case. First, the flow is initialized on two coarser grids, and then the solution is interpolated onto the finest level mesh where iterations are performed until convergence is reached. Multigrid iterations are implemented on the level 2 (medium coarse) mesh and the level 3 (fine) mesh in order to increase the convergence speed. The $\alpha = 1.0°$ case shown is with the SST model, the $\alpha = 5.0°$ case shown is with the B-B model, and the $\alpha = 10.0°$ case shown is with the S-A model. The Baldwin-Lomax with Degani-Schiff (B-L) runs were made on the Cray Y-MP at Langley Research Center, while the runs for the other three turbulence models were performed on the Numerical Aerospace Simulator (NAS) Cray C-90. All run times given in the figures are in C-90 equivalent central processing unit (CPU) hours. The jump seen for the last few iterations in the drag histories in figures 16 and 17 was caused by a correction to the method of calculating the drag coefficient in CFL3D during the course of this study.

This correction involved a change in the way the forces were integrated; therefore, the flow field itself was not affected. Since these cases were already converged when the correction was made, a few (5 to 10) iterations were run on each case, even though only one iteration was needed in order to obtain the correct drag values for these cases.

Table 1 gives a tabulated listing of the run times for all four turbulence models at all three angles of attack; all run times given are in C-90 equivalent CPU hours. The results in the table show that S-A uses the least μs/gridpoint/iteration at all three angles of attack, with B-L using the next fewest at all three angles of attack. The results in the table also show that S-A converges the fastest, in terms of CPU hour usage, of the four models at all three angles of attack. At $\alpha = 1.0°$ and $\alpha = 10.0°$, the SST model has the next fastest convergence rate, but at $\alpha = 5.0°$ B-L has the second fastest convergence rate. Finally, the results in the table show that S-A uses the lowest percentage of CPU hours on the fine mesh of the four models at all three angles of attack. At $\alpha = 1.0°$ and $\alpha = 10.0°$, the B-B model uses the next to the lowest percentage of CPU hours on the fine mesh, and at $\alpha = 5.0°$, B-L uses the second lowest percentage of CPU hours on the fine mesh. These percentages are important when considering that B-L needs 120 MW of memory to run on the fine mesh, while S-A, SST, and B-B require 127 MW, 127 MW, and 136 MW, respectively. The amount of memory each model uses is important because of the limited availability of computer resources.

Pressure comparisons. The spanwise and chordwise pressure distributions for the $\alpha = 1.0°$ case are shown in figures 19 and 20, respectively. These figures indicate that for this low angle of attack, all turbulence models agreed well with the experimental data at all six spanwise and at all three chordwise pressure stations. This behavior is expected because this relatively benign flow is mostly attached, and all models should behave the same for attached flow. The spanwise and chordwise pressure distributions for the $\alpha = 5.0°$ case are shown in figures 21 and 22, respectively. The spanwise pressure distributions for the $\alpha = 5.0°$ case shown in figure 21 indicate that up to the crank in the wing, all turbulence models predict the flow characteristics very well. At the crank region ($x = 46.5$ in.) none of the models pick up the detail seen in the outboard 20-percent span in the experimental data. At an x station of 49.55 in., B-L is the only model that picks up the apparent suction peak at 90-percent span in the experimental data. At the $x = 53.16$-in. station, all models perform equally well, with B-L showing a suction peak at approximately 80-percent span. The experimental pressures do not extend this far outboard; therefore, it is difficult to determine whether the suction peak is real. Figure 22 shows that for the $\alpha = 5.0°$ case, all four models give good agreement with experimental data at the first two y locations. At the $y = 9.95$-in. location, no models match the pressure measurement on the upper surface.

The spanwise and chordwise pressure distributions for the $\alpha = 10.0°$ case are shown in figures 23 and 24, respectively. The spanwise pressure distributions for the $\alpha = 10.0°$ case shown in figure 23 indicate that at the x station of 34.245, all models predict the flow similarly, and this prediction varies slightly from the experimental flow. At the next two stations, that is, at $x = 37.98$ in. and $x = 41.45$ in., no models pick up the magnitude of the suction peak seen at approximately 90-percent span and 85-percent span, respectively, in the experimental flow. At the crank region, that is, at $x = 46.5$ in., the B-L model overpredicts the suction peak seen at approximately 80-percent span in the experimental data by approximately the same amount that the other three models underpredict the height of the suction peak. At an x station of 49.55 in., B-L comes the closest to matching the fluctuations in the experimental data. At the $x = 53.16$-in. station, B-L comes the closest of the four models to picking up the upper surface pressure distribution seen in the experiment. Figure 24 shows that for the $\alpha = 10.0°$ case, no models pick up the dip in the pressure curve which occurs at 60-percent chord in the experimental data at the $y = 3.036$-in. station. At the second y location, $y = 5.544$ in., B-L comes the closest to picking up the drop in the pressure curve at 30-percent chord, but all four models pick up the pressure at 60-percent chord. At the $y = 9.95$-in. location, all models come close to predicting the experimental value for the upper surface pressure; B-L shows some fluctuations in the pressure distribution which the other models do not predict. There is no way of knowing whether these fluctuations really do occur in nature because there were no pressure values taken experimentally.

Surface streamlines. Figures 25 through 27 show the computational surface streamlines for the $\alpha = 1.0°$, 5.0°, and 10.0° cases, respectively, for all four turbulence models. In these figures, a separation line is indicated by the streamlines coalescing to a line, while an attachment line is a line from which the streamlines are flowing. As shown in figure 25, the computational surface streamlines are aligned with the free-stream flow on both the outboard and inboard wing sections for all four turbulence models at $\alpha = 1.0°$. The data indicate there is no separation present at this low angle of attack. In figure 26, all computational surface streamlines for the $\alpha = 5.0°$ case show a separation at the crank with an attachment near the outboard wing leading edge. The B-L solution shows an additional separation and reattachment at the outboard wing leading edge that the other models do not show. Figure 27 shows the computational streamlines for the $\alpha = 10.0°$ case. All models show a separation at the crank region of the wing. The B-L case, however, also shows a separation at the inboard leading edge of the wing and a reattachment line in the outboard region of the wing. The other three models show a separation region at the tip of the wing that the B-L model does not show. No experimental data are available for comparison.

Force and moment comparisons. Figures 28 through 31 show the drag polars, lift-to-drag ratios, lift curves, and pitching-moment curves, respectively, for the four different turbulence models and the experimental data. Table 2 shows the data which are plotted, and table 3 gives a numerical breakdown of the pressure drag and viscous drag components for all calculations made for this study. Figure 28 shows the drag polar for the four different turbulence models and the experimental data. At $\alpha = 1.0°$, all turbulence models predict the lift-to-drag ratio to within the accuracy of the experimental drag value (i.e., ±0.0003). At the design point, $\alpha = 5.0°$, B-B is approximately 8 drag counts low, with S-A, SST, and B-L being 10, 11, and 15 drag counts low, respectively. At $\alpha = 10.0°$, B-L predicts lift and drag lower than the other three models, but it does come the closest to predicting the ratio of lift to drag.

The computational wing pressure distributions discussed earlier in this paper indicated that B-L agreed the best with the experimental data while the drag data in figure 28 indicate that the B-B model agrees somewhat better with the experiment at $\alpha = 5.0°$. This discrepancy is probably caused by a difference in the viscous drag components of the turbulence model results, which are shown in table 3. The B-L turbulence model viscous-drag-component results are approximately 10 drag counts lower than the other three models at all three angles of attack. At $\alpha = 10.0°$, the pressure component of drag for B-L is approximately 60 drag counts lower than the other three models. This factor can account for the results seen at this angle of attack. Note also that the equivalent flat plate viscous drag $C_{D_v} = 0.0064$ for $M = 0.90$ and $\mathrm{Re}_{\bar{c}} = 30 \times 10^6$, which is 7 to 17 counts higher than the computations herein. Figure 32 shows that if the flat plate equivalent viscous-drag component is substituted for the computational viscous-drag component, the computational data agree much better with the experimental data.

The lift-to-drag ratios for the four turbulence models versus the experimental data are shown in figure 29. This figure shows that at $\alpha = 1.0°$, all four models predict approximately the same *L/D* value, which agrees well with the experimental value. At $\alpha = 5.0°$, B-B comes closest to matching the experimental data. At $\alpha = 10.0°$, B-L predicts the experimental *L/D* level closer than the other three models. The discrepancies between the computational and experimental pressure data previously examined and the force data comparisons shown here are consistent with the differences in the viscous drag and pressure drag components of the four turbulence models.

Figure 30 shows the lift curve for the four turbulence models and the experimental data. At $\alpha = 1.0°$, all models are slightly higher than the experimental data. At the design point, $\alpha = 5.0°$, B-L is closer to the experimental lift curve than the other three models, and at $\alpha = 10.0°$, B-L is again closer to the experimental lift curve than the other three models.

Figure 31 shows the pitching-moment curves for the four turbulence models and the experimental data. At $\alpha = 1.0°$, all models underpredict the pitching moment. At $\alpha = 5.0°$, all models again underpredict the

pitching moment, but B-L comes the closest to the experimental values. At $\alpha = 10.0°$, all models again underpredict the pitching moment, but B-L comes the closest to the experimental values.

These results show that the computed forces and pressure compared reasonably well with the experimental data, with the B-L and B-B models showing superior agreement. None of the turbulence models predict the experimental flow well at all conditions tested herein. B-L seems to give the best agreement with the force data at the higher angles of attack, while B-B agrees better with the force data at lower angles of attack. Also, substitution of the theoretical equivalent flat plate C_{D_v} for the Navier-Stokes computed C_{D_v} significantly improves the agreement between the computational and the experimental data.

Conclusions

Four turbulence models, the equilibrium model of Baldwin-Lomax (B-L) with the Degani-Schiff (D-S) modifications, the one-equation Baldwin-Barth (B-B) model, the one-equation Spalart-Allmaras (S-A) model, and Menter's two-equation Shear Stress Transport model (SST) have been evaluated for transonic flow over a high-speed research (HSR) geometry using the thin-layer, upwind, Navier-Stokes flow solver known as CFL3D. The flow conditions tested were a Mach number of 0.90 and a Reynolds number of 30×10^6 based on chord for a range of angles of attack of 1°, 5°, and 10° which correspond to tests performed in the National Transonic Facility (NTF) at Langley Research Center. The results indicate that either a C-O topology or an O-C topology will give reasonable results for this configuration, but the C-O topology was found to be slightly better. In addition, the detail of the geometric modeling of the blunt-to-sharp leading-edge transition at the wing crank did not significantly affect the results, at least for the variation of detail examined herein. A distance function modification within CFL3D improved correlation between the S-A and Menter's SST turbulence model results. The turbulence model study showed that the computed forces and pressure compared reasonably well with the experimental data. Finally, the results also showed that S-A converges the fastest of the four models at all three angles of attack.

NASA Langley Research Center
Hampton, VA 23681-2199
June 17, 1997

References

1. Wood, Richard M.: *First NASA/Industry High-Speed Research Configuration Aerodynamics Workshop.* NASA/CP-1999-209690, 1999.

2. Thomas, James L.; Anderson, W. Kyle; and Krist, Sherrie Taylor: Navier-Stokes Computations of Vortical Flows Over Low-Aspect-Ratio Wings. *AIAA J.*, vol. 28, Feb. 1990, pp. 205–212.

3. Spalart, P. R.; and Allmaras, S. R.: A One-Equation Turbulence Model for Aerodynamic Flows. AIAA-92-0439, Jan. 1992.

4. Baldwin, B.; and Lomax, H.: Thin-Layer Approximation and Algebraic Model for Separated Turbulent Flows. AIAA-78-257, Jan. 1978.

5. Degani, David; Schiff, Lewis B.; and Levy, Yuval: Physical Considerations Governing Computation of Turbulent Flows Over Bodies at Large Incidence. AIAA-90-0096, Jan. 1990.

6. Baldwin, Barrett; and Barth, Timothy J.: *A One-Equation Turbulence Transport Model for High Reynolds Number Wall-Bounded Flows.* NASA TM-102847, 1990.

7. Menter, F. R.: Two-Equation Eddy-Viscosity Turbulence Models for Engineering Applications. *AIAA J.*, vol. 32, no. 8, Aug. 1994, pp. 1598–1605.

8. Roe, P. L.: Approximate Riemann Solvers, Parameter Vectors, and Difference Schemes. *J. Comput. Phys.*, vol. 43, Oct. 1981, pp. 357–372.

9. Steinbrenner, John P.; and Chawner, J. R.: *The GRIDGEN Version 8 Multiple Block Grid Generation Software.* MDA Eng. Rep. 92-01, Dec. 1992.

Table 1. Tabulated Run Times

α, deg	Turbulence model	μs/gridpoint/ iteration	CPU hr (C-90 equiv.)	CPU hr used on fine mesh, percent
1	B-L	13.12	6.77	87
1	B-B	13.99	7.80	80
1	S-A	10.14	4.90	77
1	SST	14.54	6.29	86
5	B-L	11.05	5.52	89
5	B-B	12.12	9.74	93
5	S-A	10.18	4.91	77
5	SST	12.56	11.31	91
10	B-L	10.75	10.58	91
10	B-B	14.10	10.64	89
10	S-A	10.19	4.92	77
10	SST	13.97	10.29	91

Table 2. Tabulated Values of Drag, Lift, and Pitching Moment

Force	α, deg	Exp. $q = 1005$	Baldwin-Lomax	Baldwin-Barth	Spalart-Allmaras	Menter's SST
C_D	1	0.0074	0.0054	0.0062	0.0063	0.0060
	5	.0183	.0176	.0191	.0188	.0185
	10	.0751	.0768	.0847	.0855	.0855
C_L	1	−.008	.001	.002	.002	.001
	5	.217	.226	.232	.232	.230
	10	.494	.496	.542	.548	.550
C_m	1	.014	.011	.011	.011	.011
	5	.008	.006	.004	.004	.004
	10	.006	.004	−.007	−.009	−.010

Table 3. Tabulated Values of Computational Pressure and Viscous Drag
[Equivalent Flat-Plate Viscous Drag; $M = 0.90$; $\mathrm{Re}_{\bar{c}} = 30 \times 10^6$; $C_{Dv} = 0.0064$]

Force	α, deg	Baldwin-Lomax	Baldwin-Barth	Spalart-Allmaras	Menter's SST
C_{D_p}	1	0.0004	0.0005	0.0005	0.0005
	5	.0130	.0135	.0133	.0131
	10	.0723	.0789	.0800	.0801
C_{D_v}	1	.0049	.0057	.0058	.0054
	5	.0046	.0056	.0055	.0053
	10	.0045	.0057	.0055	.0052

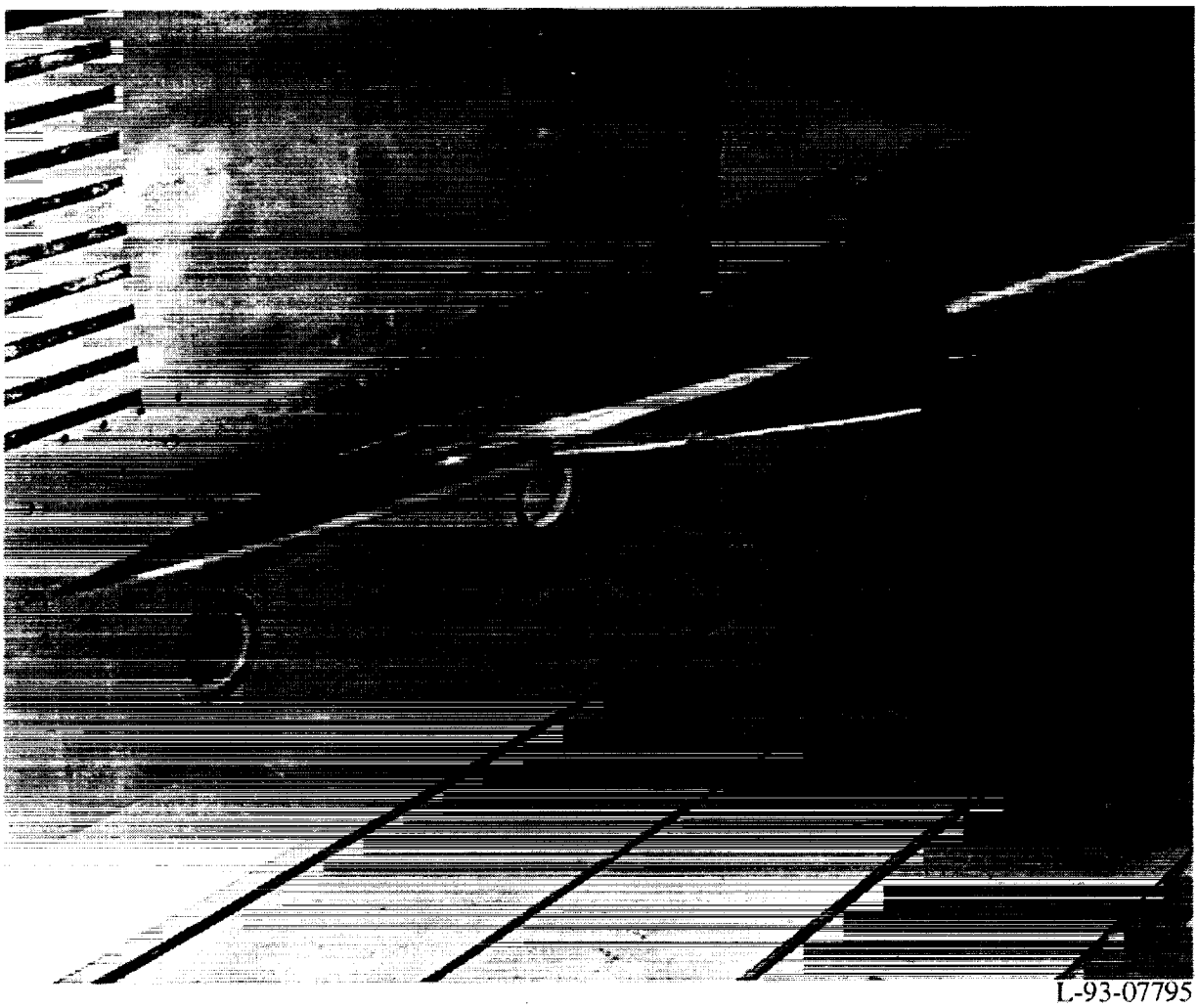

L-93-07795

Figure 1. Experimental model in the National Transonic Facility.

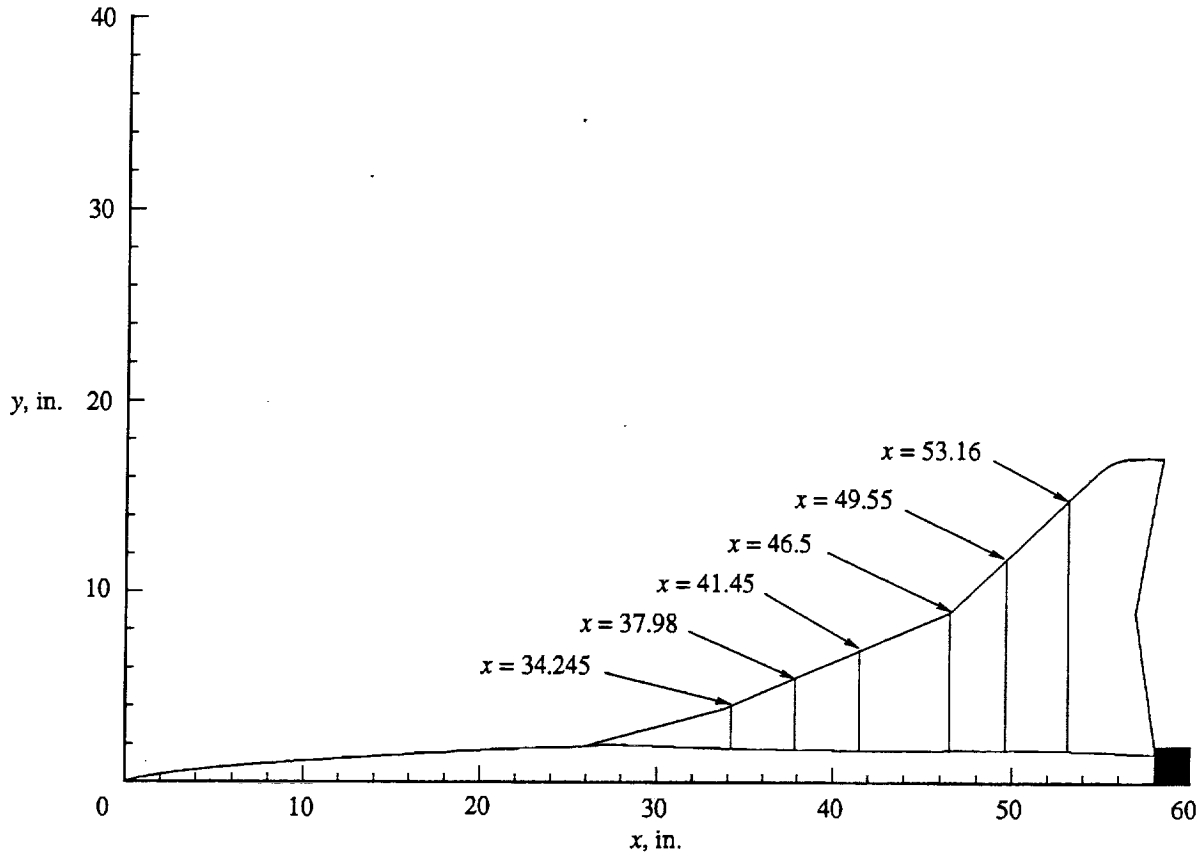

Figure 2. Spanwise pressure stations on wing of NTF 2.2-percent HSR geometry.

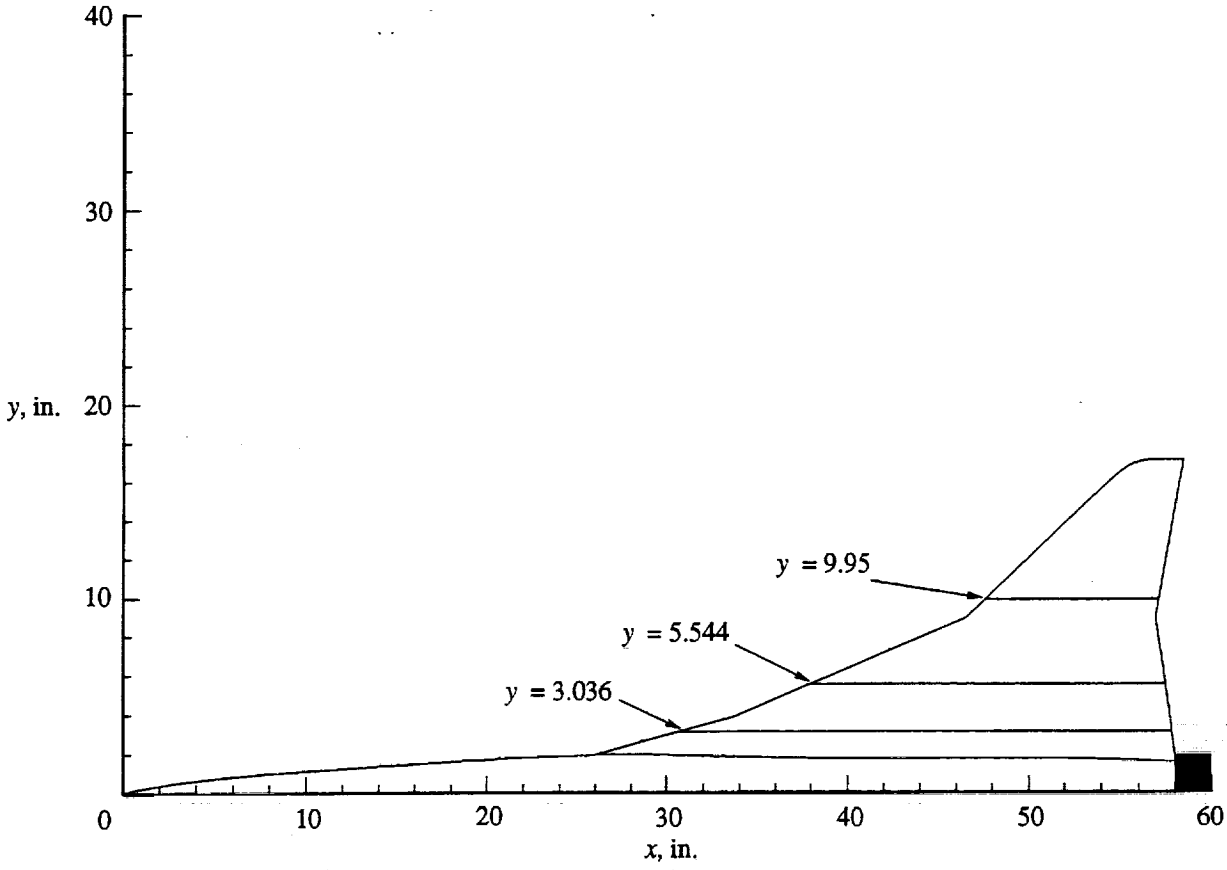

Figure 3. Chordwise pressure stations on wing of NTF 2.2-percent HSR geometry.

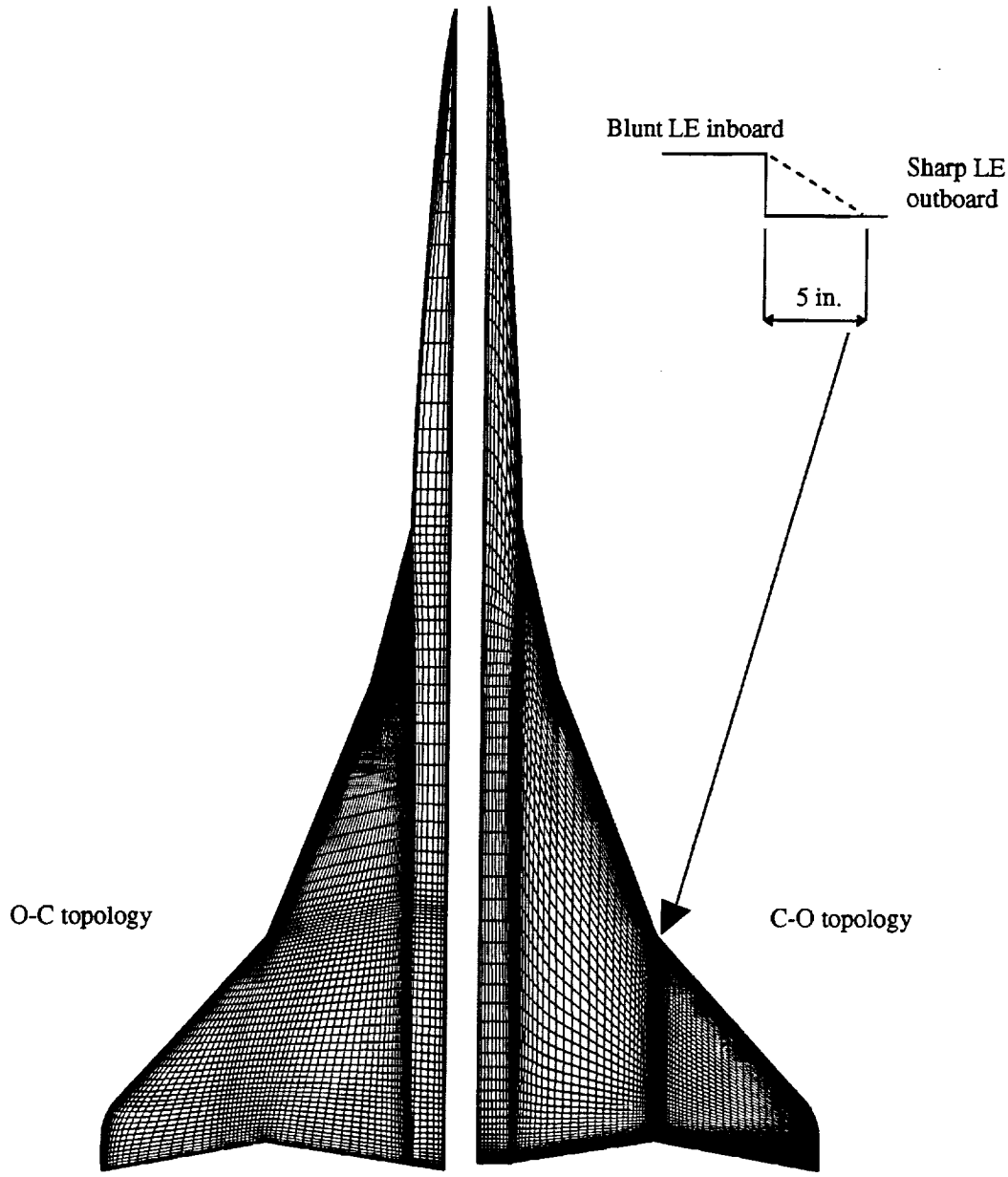

Figure 4. Wire-frame surface grids of O-C and C-O topologies.

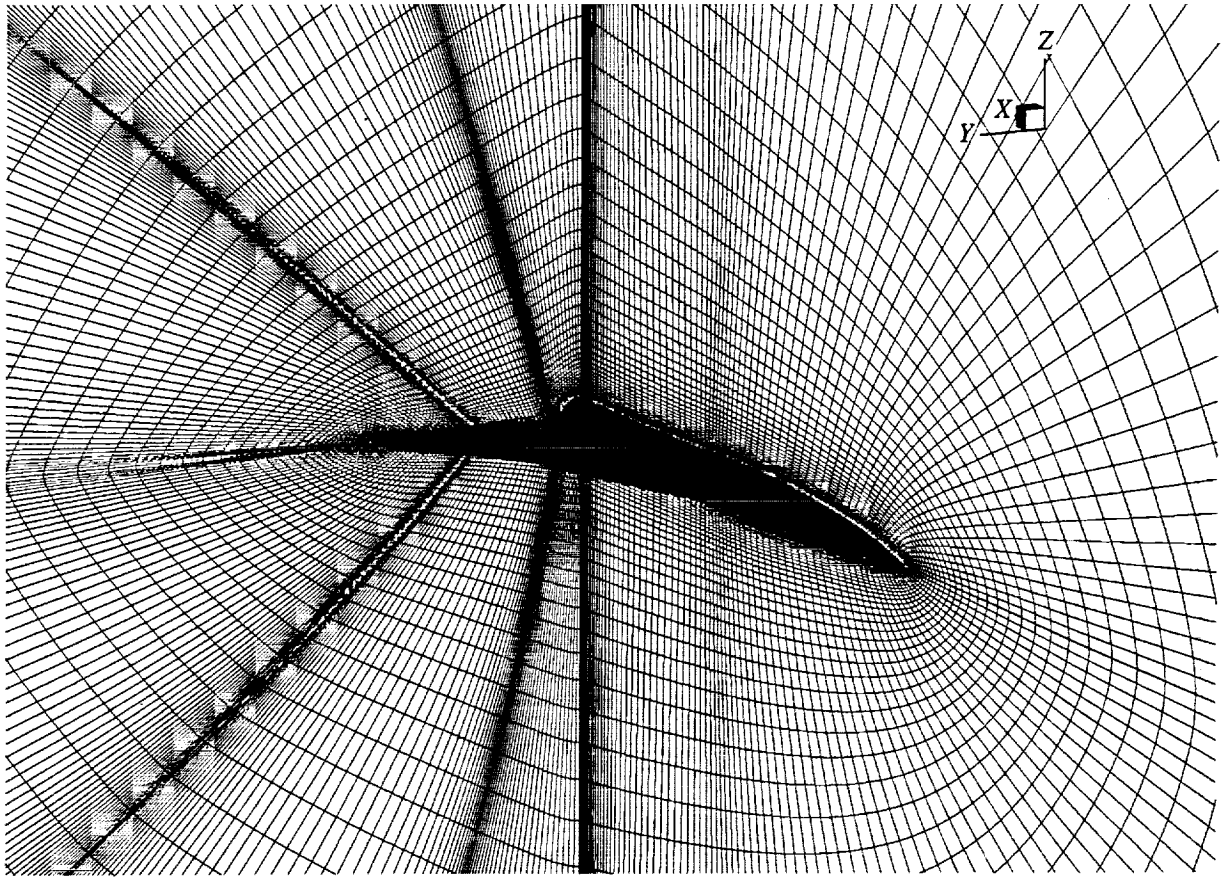

Figure 5. Representation of the C-O type volume grid for NTF 2.2-percent HSR geometry.

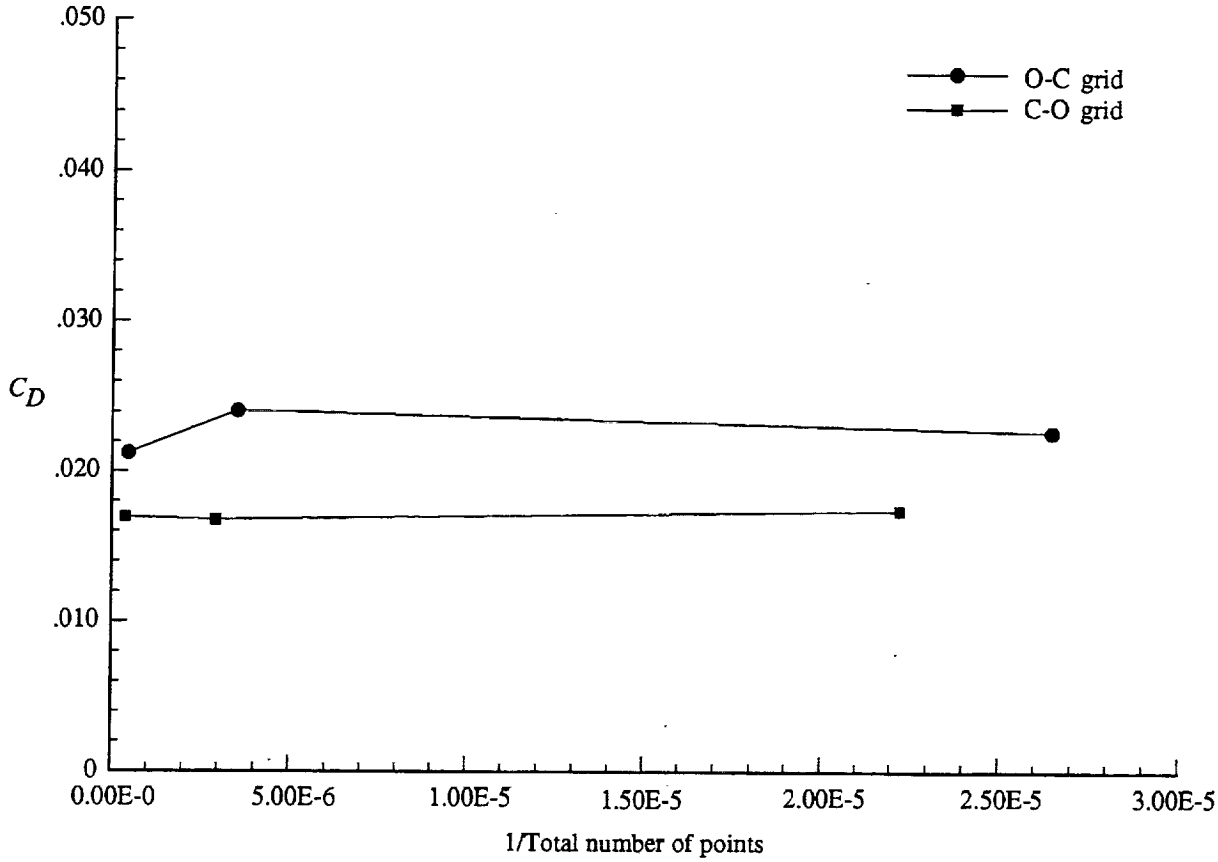

Figure 6. Grid density study showing computed drag coefficient plotted against inverse of mesh size for O-C and C-O topologies. $M = 0.90$; $\alpha = 5.0°$; $\mathrm{Re}_{\bar{c}} = 30 \times 10^6$.

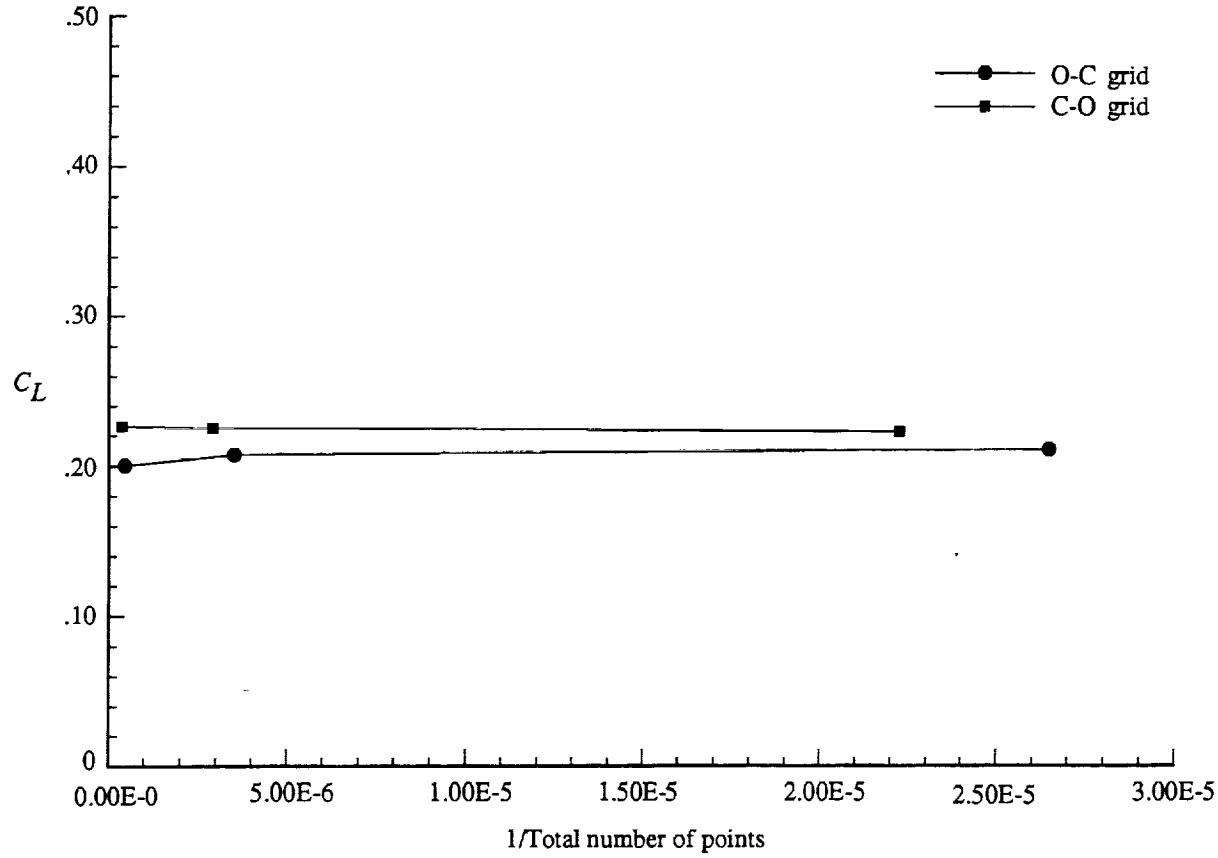

Figure 7. Grid density study showing computed lift coefficient plotted against inverse of mesh size for O-C and C-O topologies. $M = 0.90$; $\alpha = 5.0°$; $\mathrm{Re}_{\bar{c}} = 30 \times 10^6$.

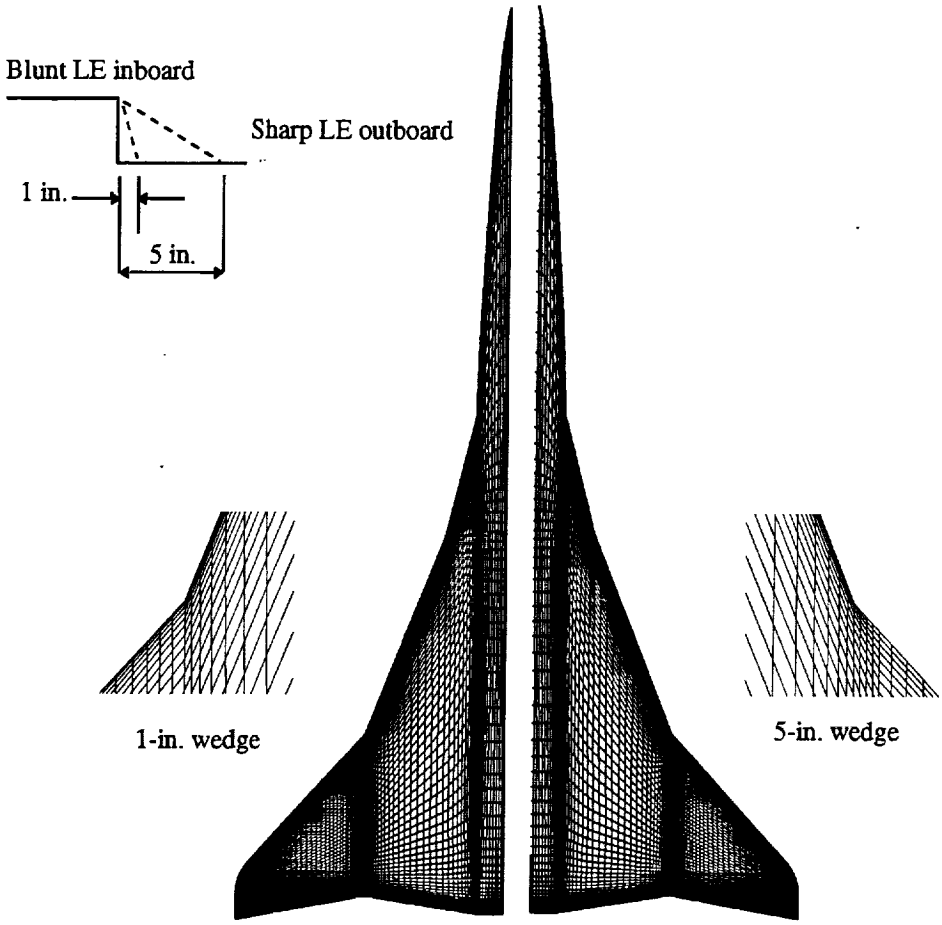

Figure 8. Wire-frame surface grids of C-O topology: 1-in. wedge and 5-in. wedge.

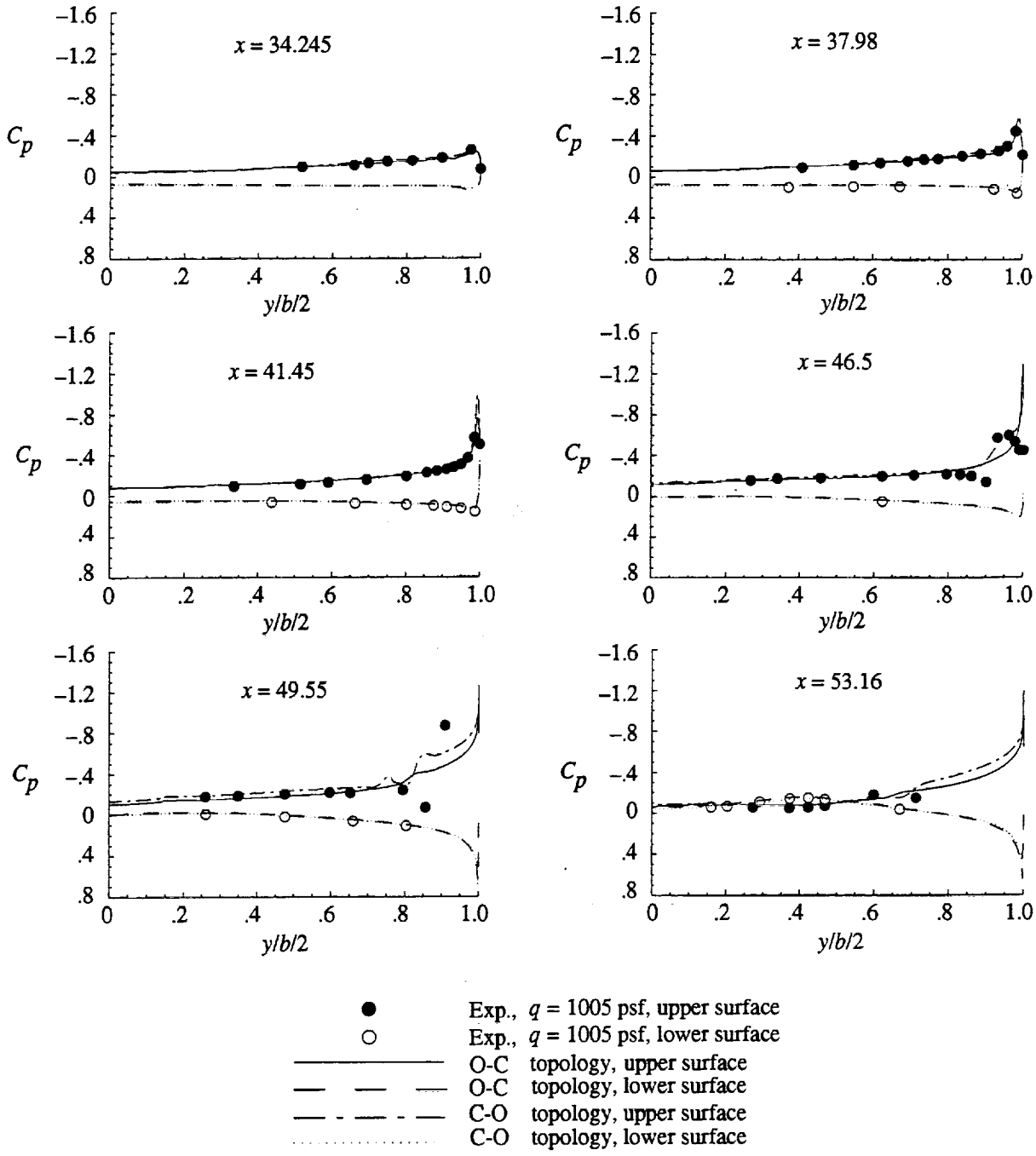

Figure 9. Surface pressure comparison between experiment, O-C, and C-O grid topology results. $M = 0.90$; $\alpha = 5.0°$; $Re_{\bar{c}} = 30 \times 10^6$. Dimensions are in inches.

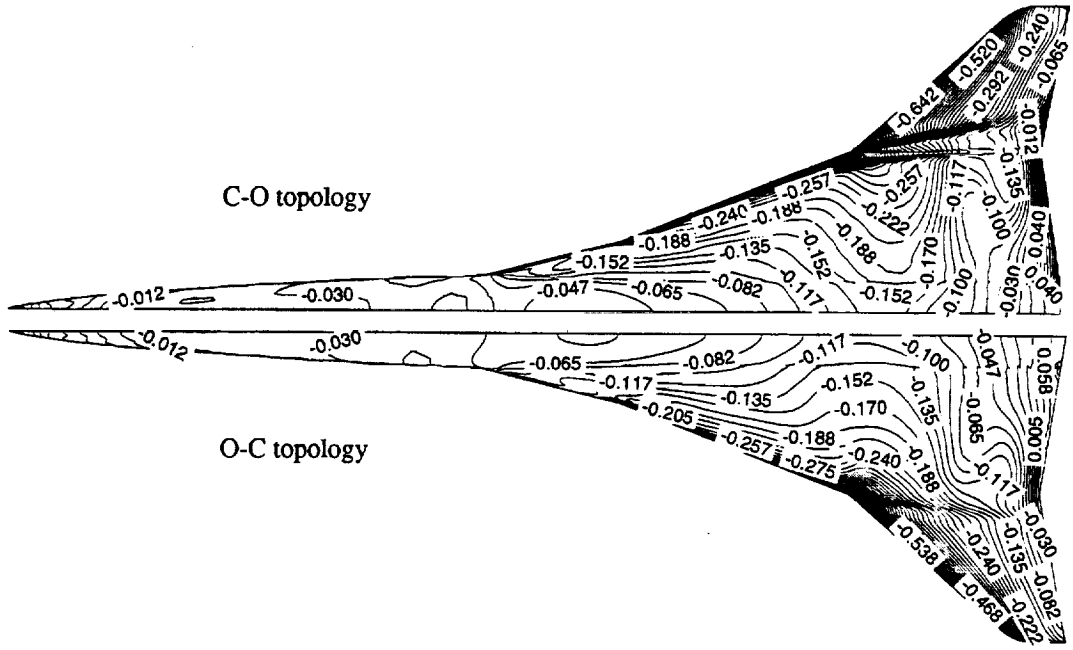

Figure 10. Pressure contour comparison between O-C and C-O grid topologies for Spalart-Allmaras turbulence model. $M = 0.90$; $\alpha = 5.0°$; $Re_{\bar{c}} = 30 \times 10^6$.

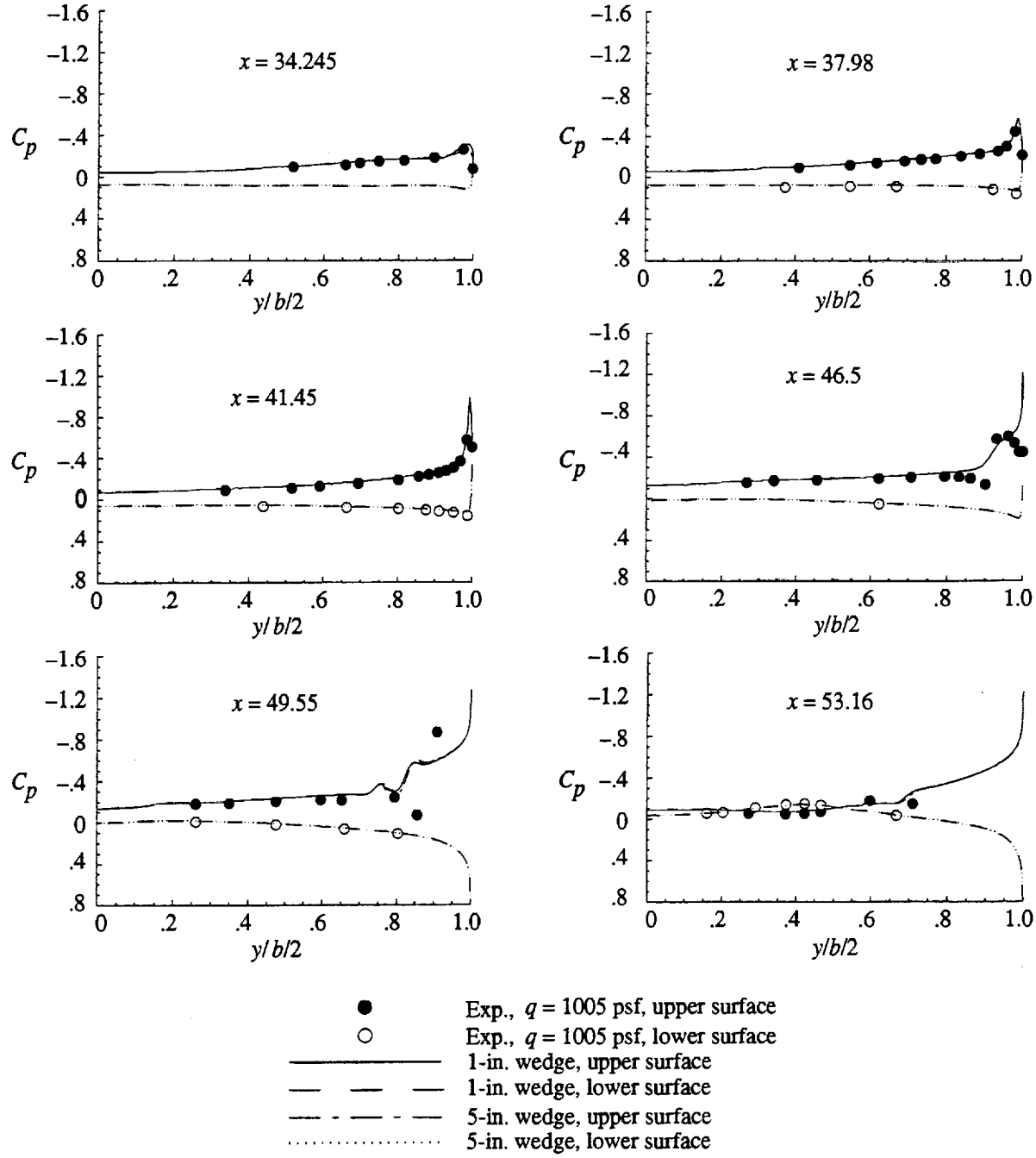

Figure 11. Surface pressure comparison between experiment, 1-in., and 5-in. full-scale wedge results. $M = 0.90$; $\alpha = 5.0°$; $Re_{\bar{c}} = 30 \times 10^6$. Dimensions are in inches.

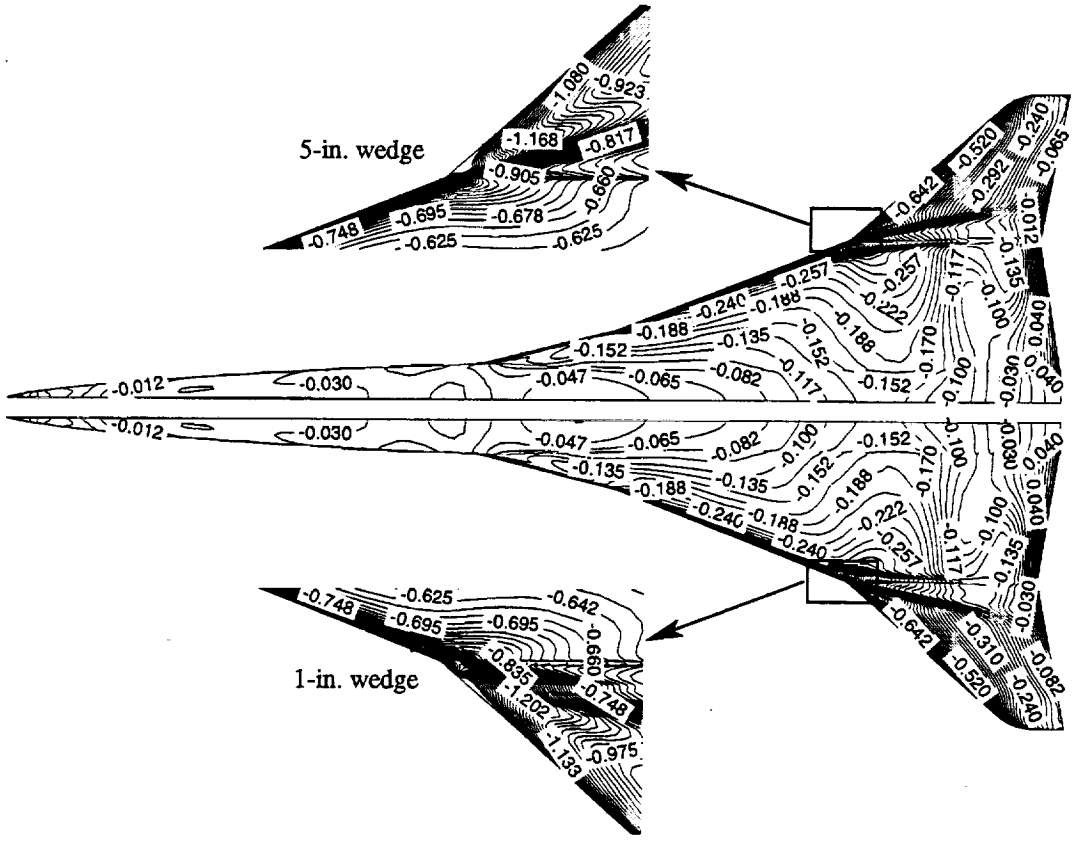

Figure 12. Pressure contour comparison between 1-in. and 5-in. full-scale wedges for Spalart-Allmaras turbulence model. $M = 0.90$; $\alpha = 5.0°$; $\mathrm{Re}_{\bar{c}} = 30 \times 10^6$.

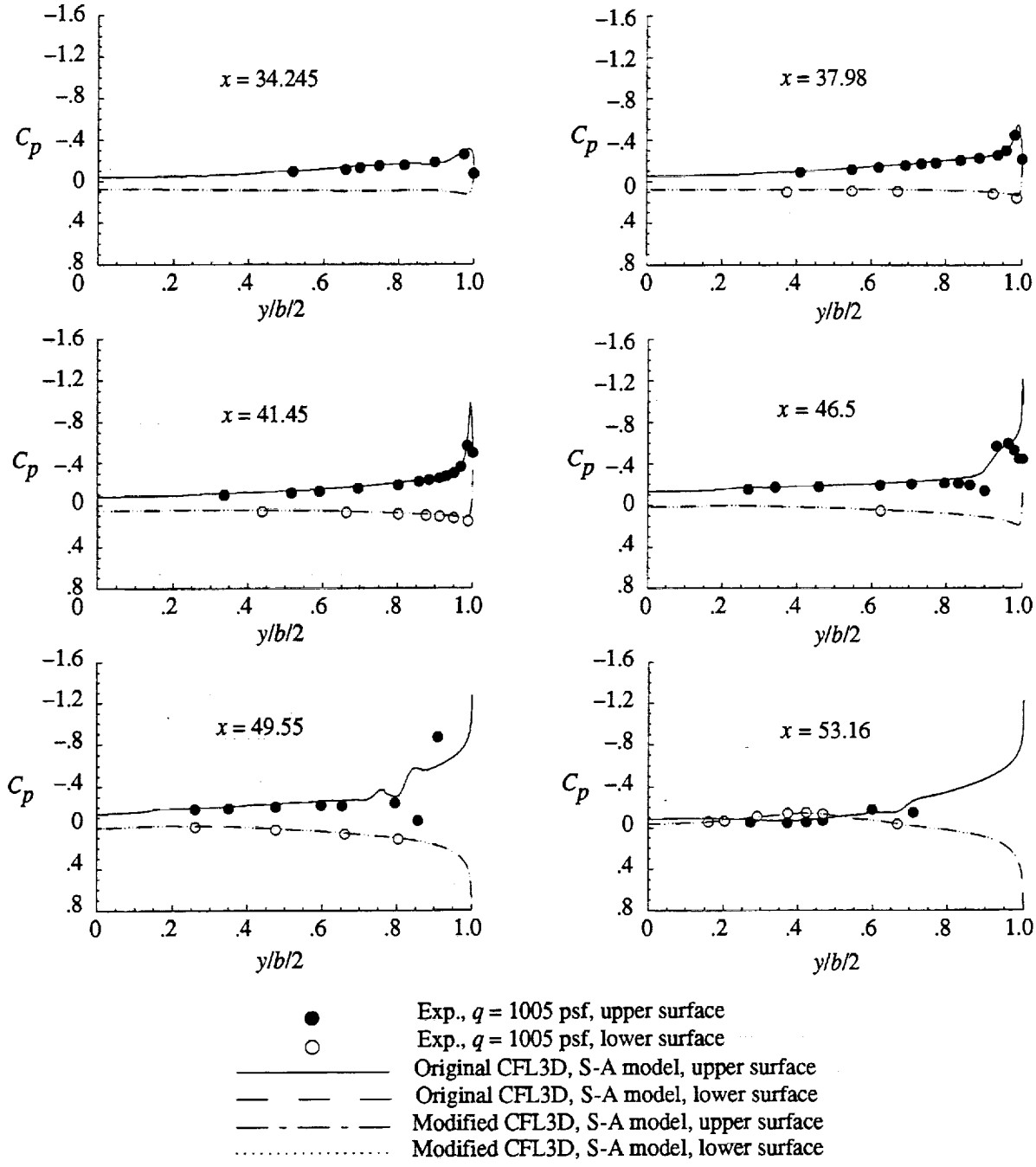

Figure 13. Code comparison, with and without modified distance function, for Spalart-Allmaras turbulence model. $M = 0.90$; $\alpha = 5.0°$; $Re_{\bar{c}} = 30 \times 10^6$. Dimensions are in inches.

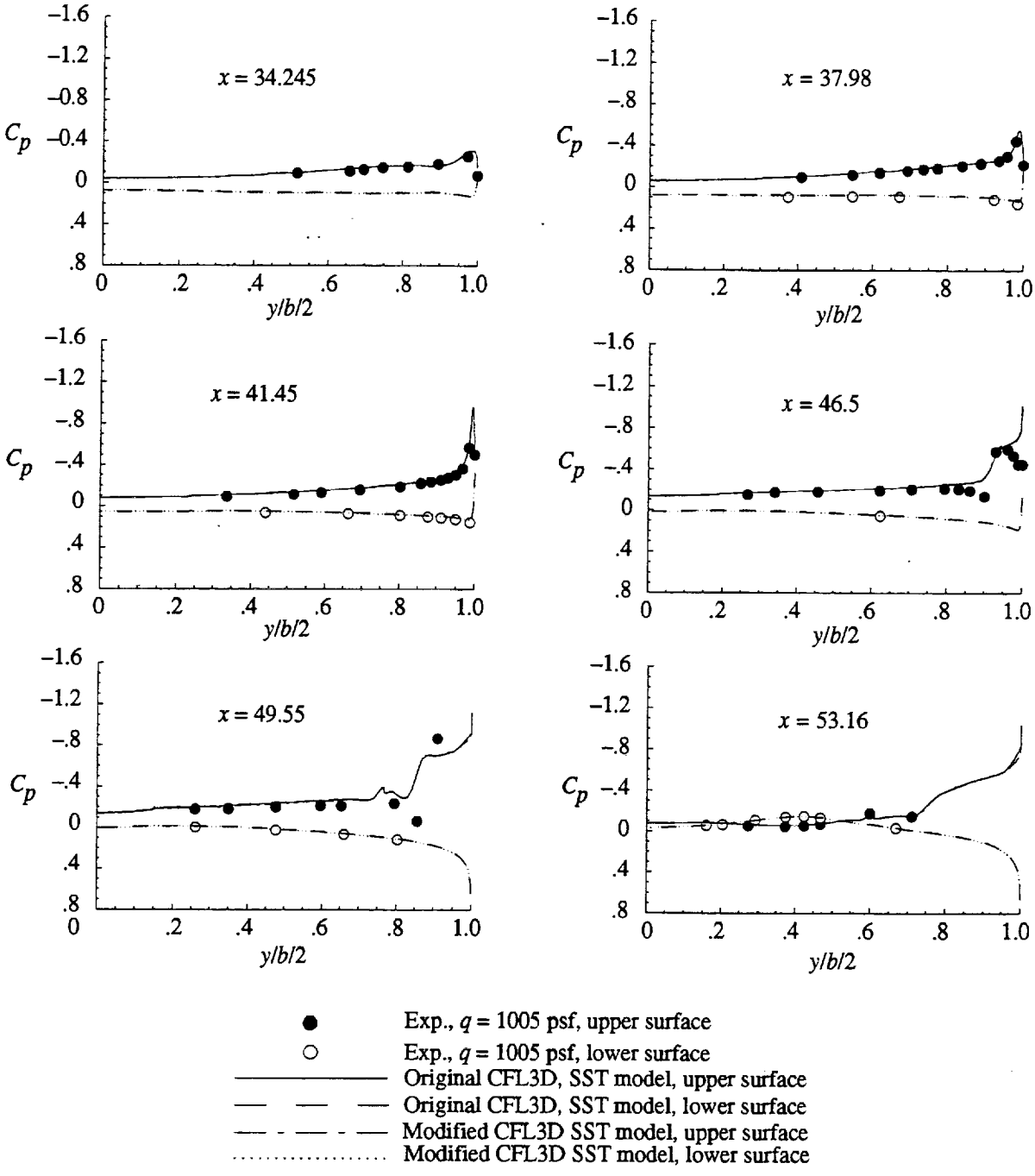

Figure 14. Code comparison, with and without modified distance function for Menter's SST turbulence model. $M = 0.90$; $\alpha = 5.0°$; $Re_c = 30 \times 10^6$. Dimensions are in inches.

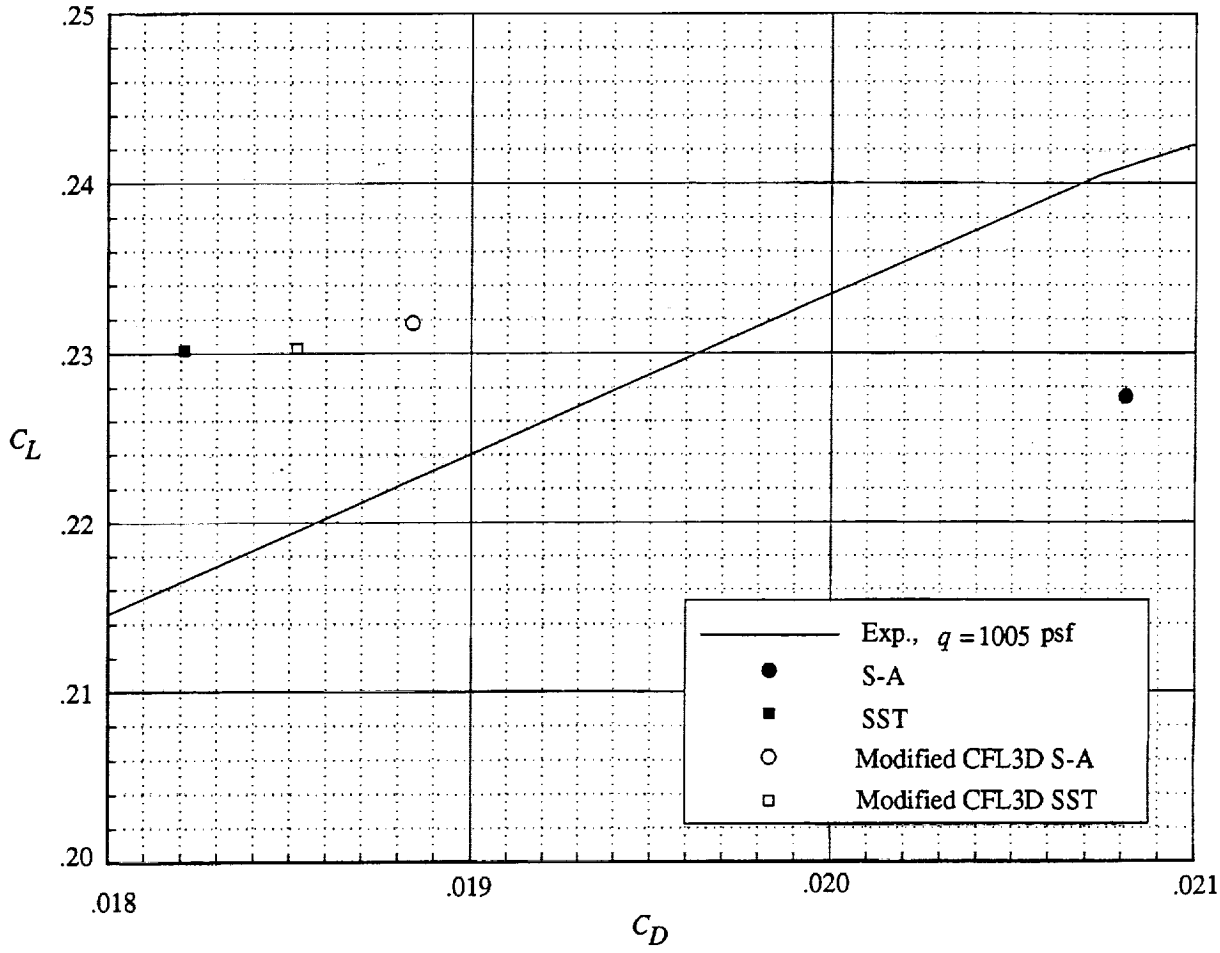

Figure 15. Drag polar for code-to-code comparisons with and without modified distance function. $M = 0.90$; $\alpha = 5.0°$; $\mathrm{Re}_{\bar{c}} = 30 \times 10^6$.

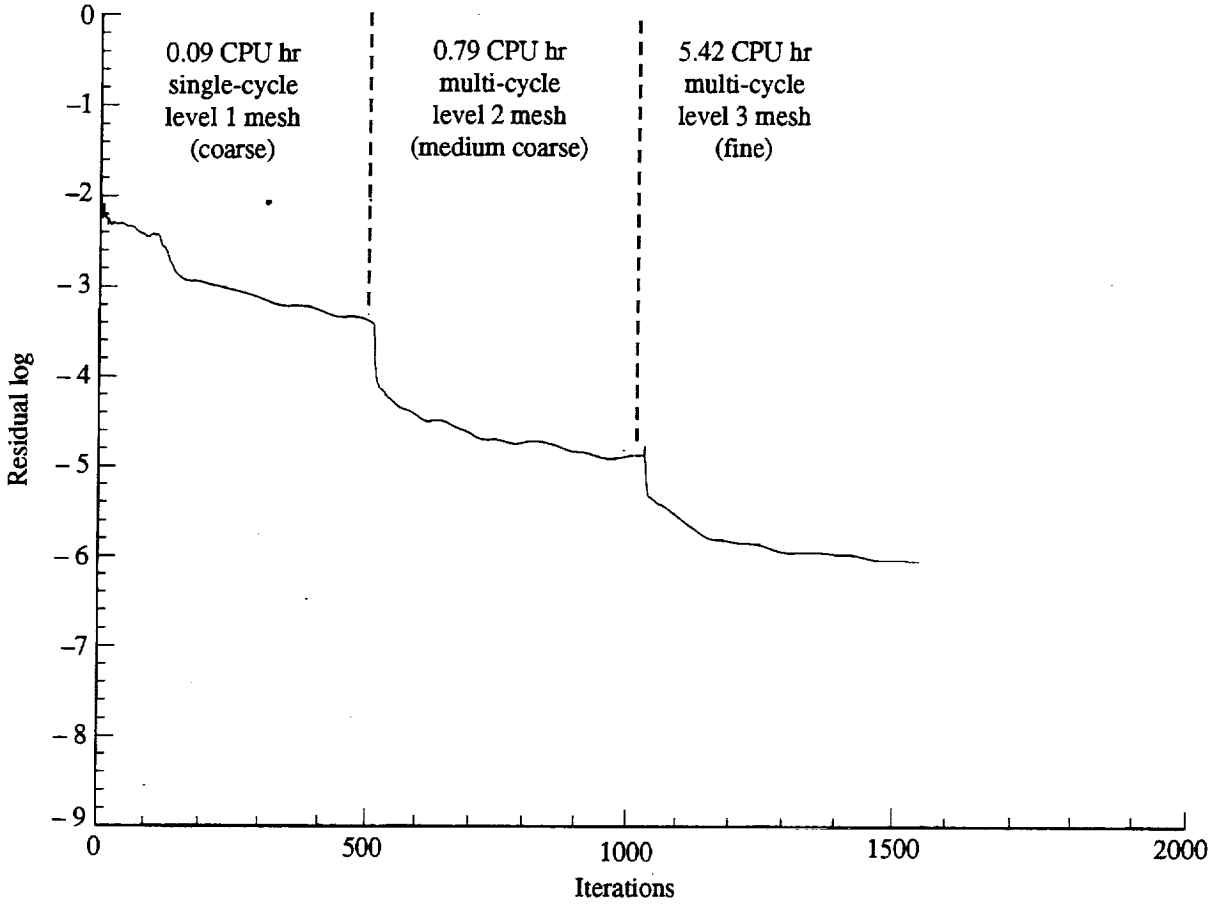

(a) Residual history.

Figure 16. Typical convergence history for $\alpha = 1.0°$ case, SST turbulence model; total CPU hours = 6.29.

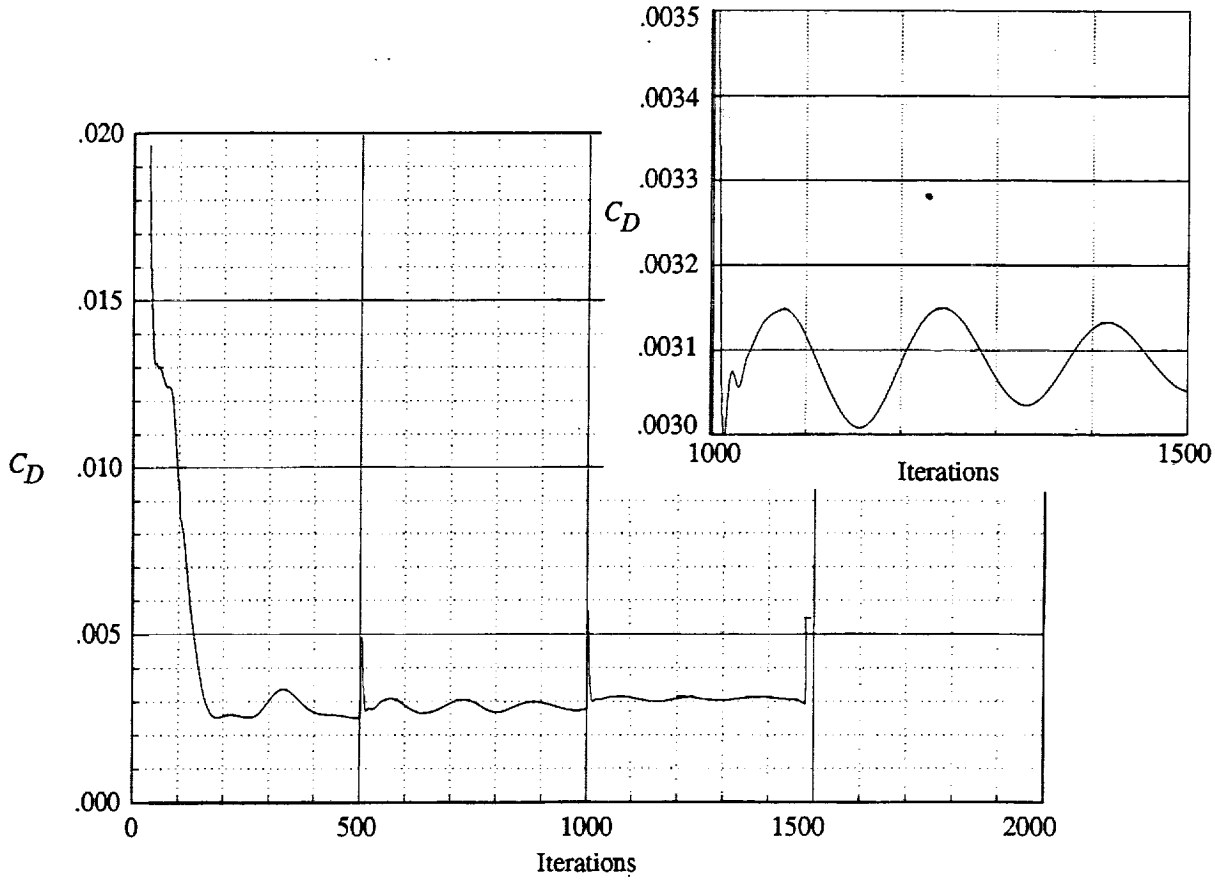

(b) Drag history.

Figure 16. Concluded.

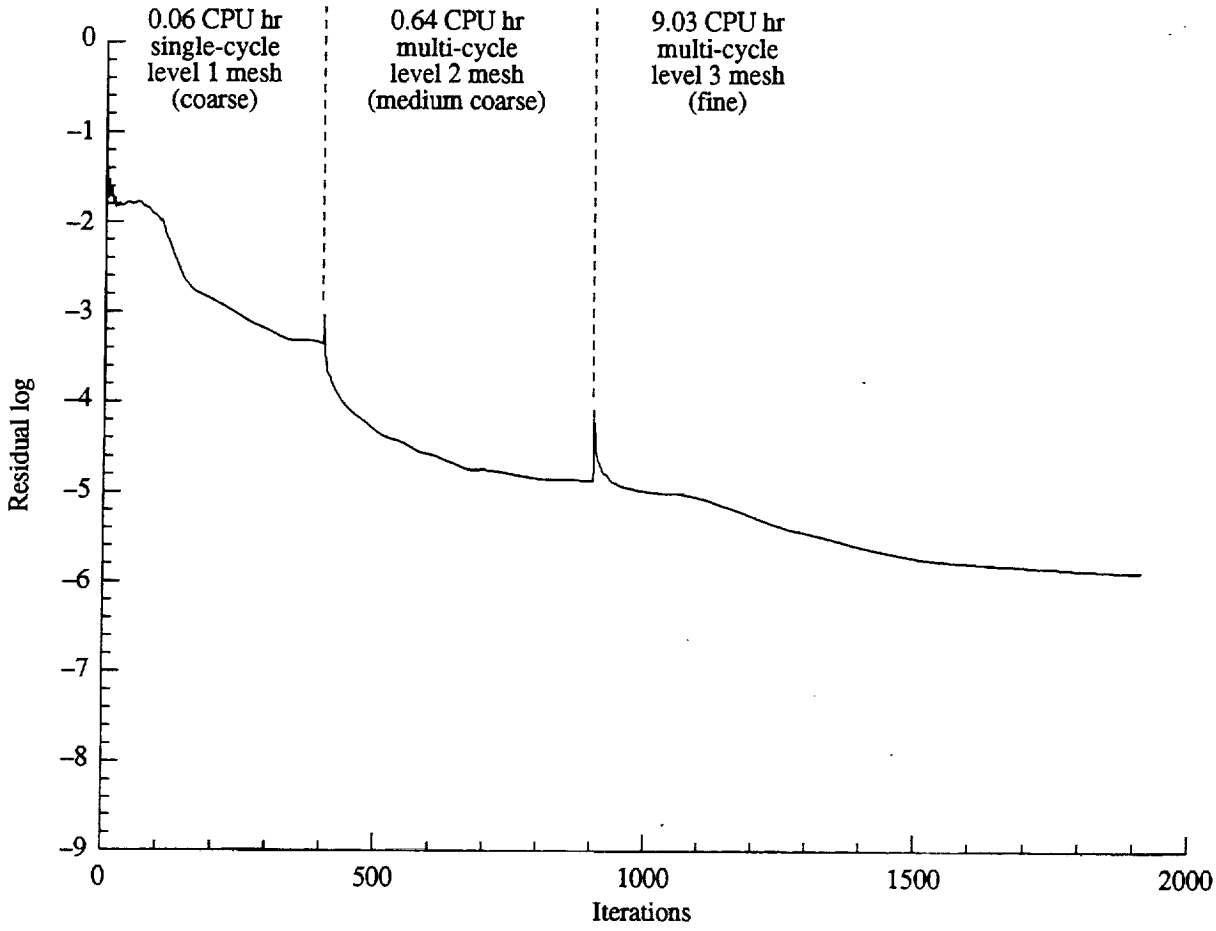

(a) Residual history.

Figure 17. Typical convergence history for α = 5.0° case, B-B turbulence model; total CPU hours = 9.74.

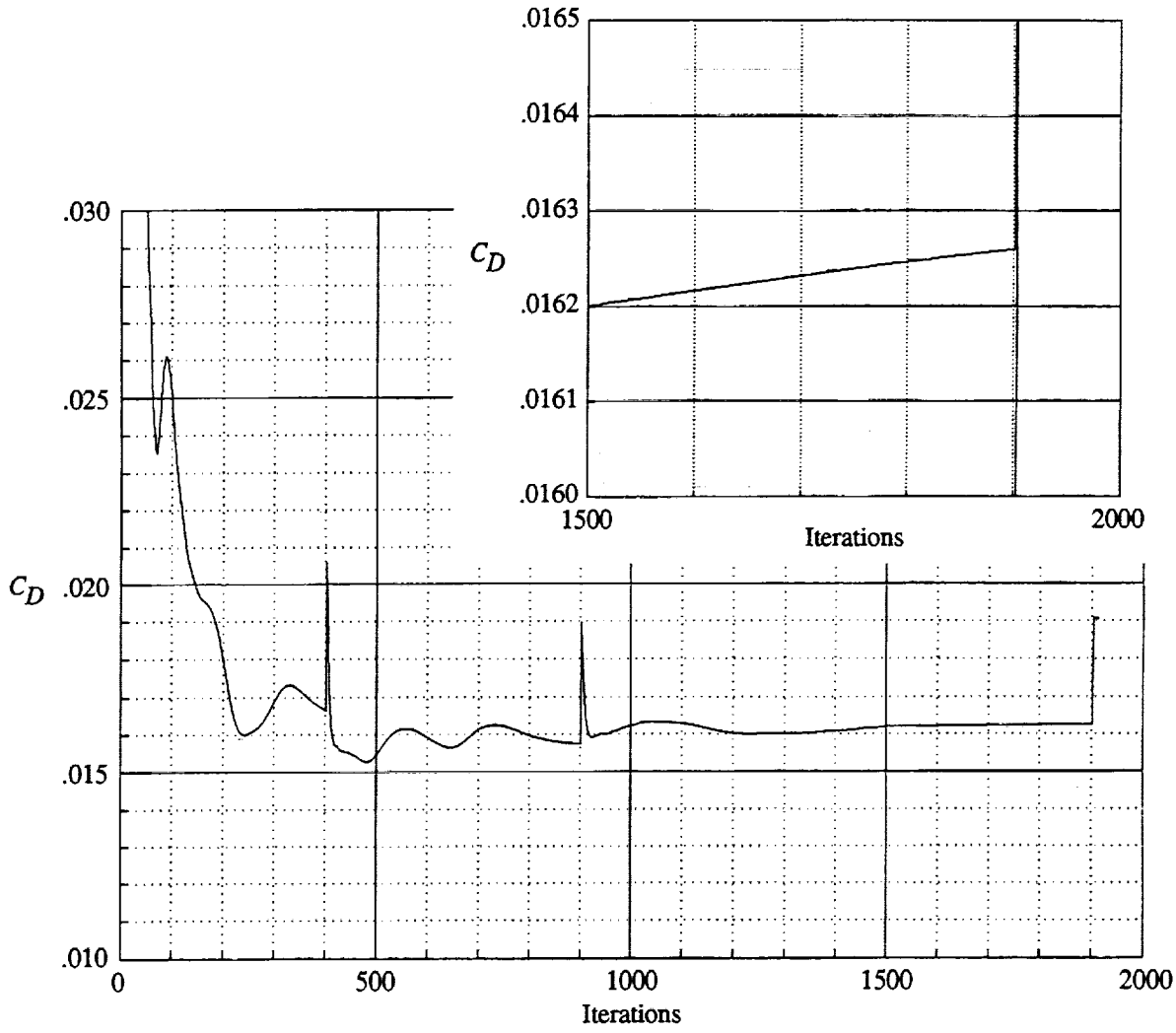

(b) Drag history.

Figure 17. Concluded.

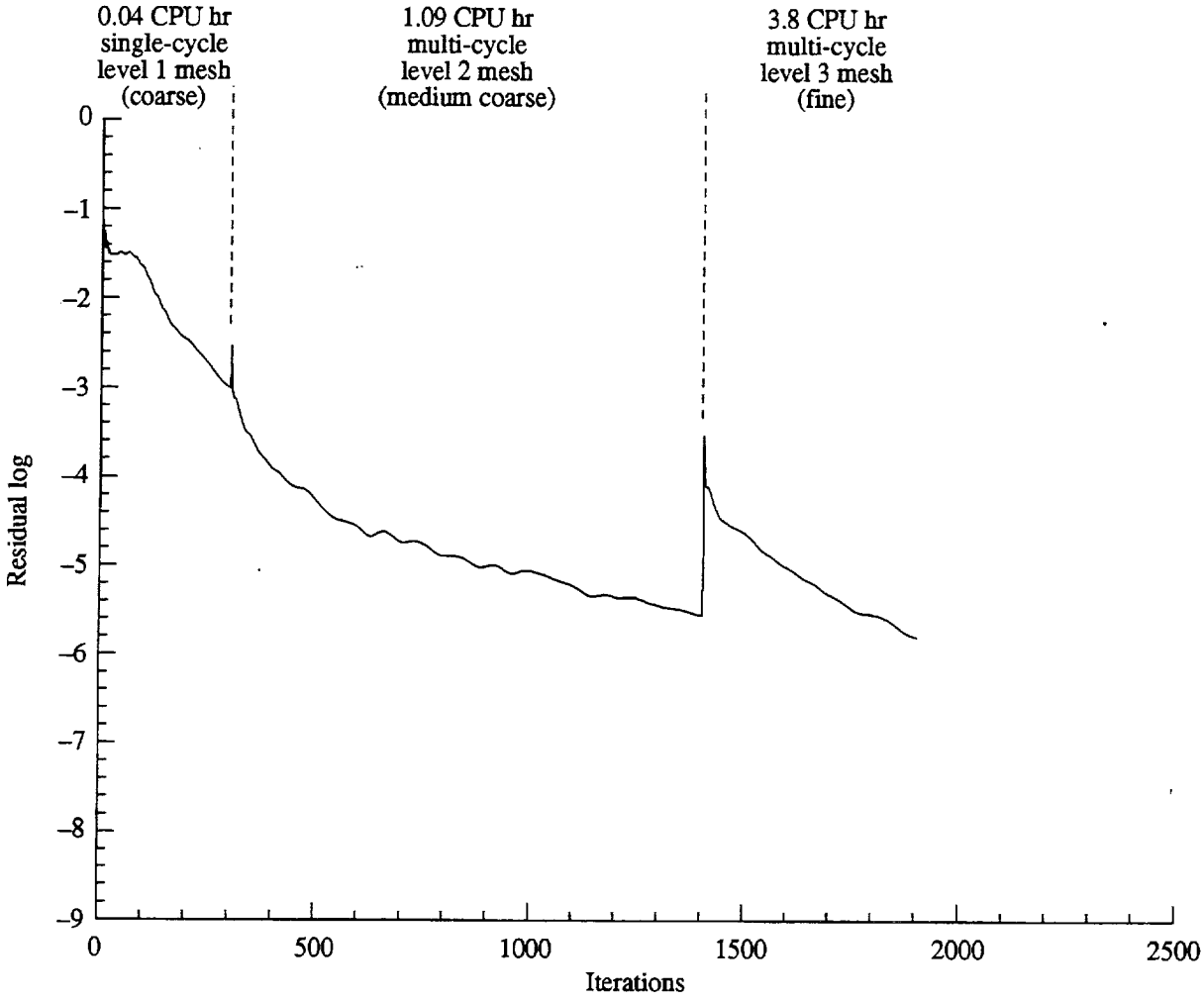

(a) Residual history.

Figure 18. Typical convergence history for $\alpha = 10.0°$ case, S-A turbulence model; total CPU hours = 4.9.

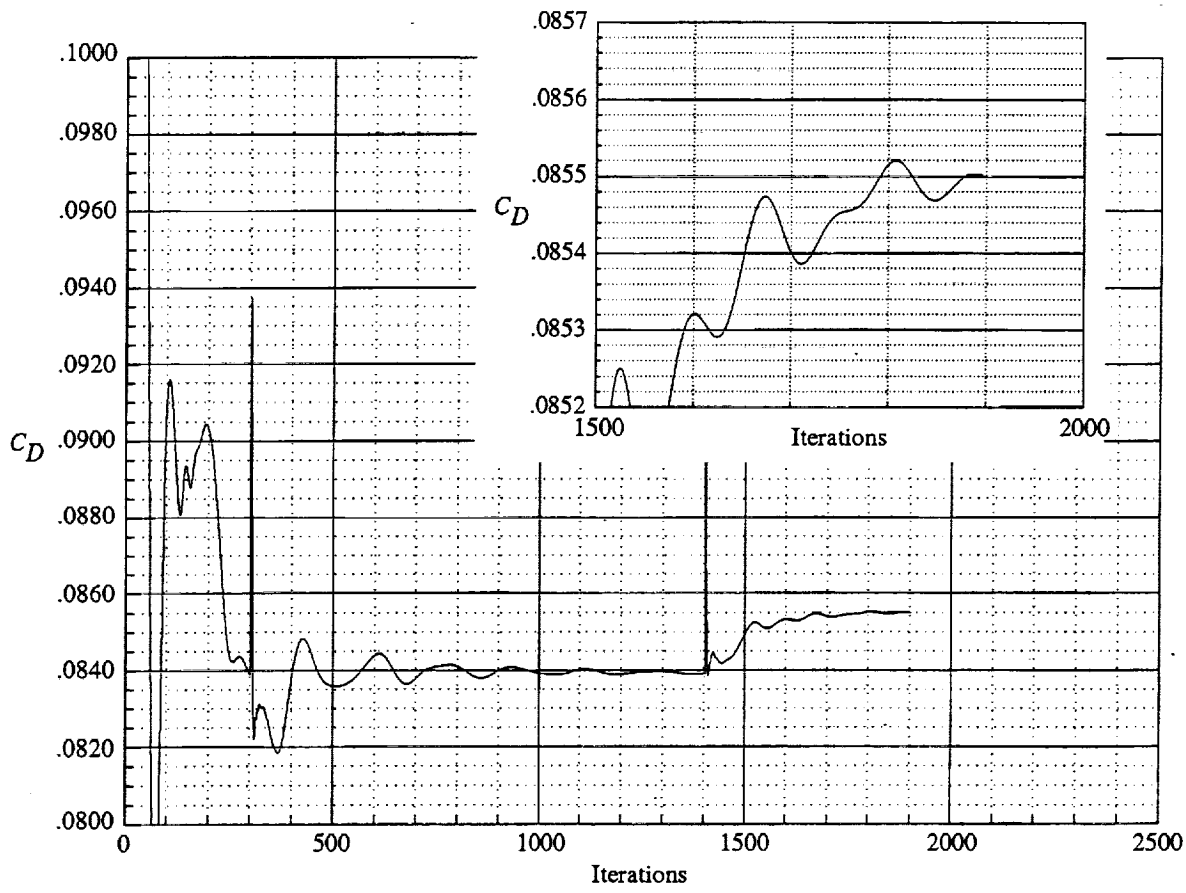

(b) Drag history.

Figure 18. Concluded.

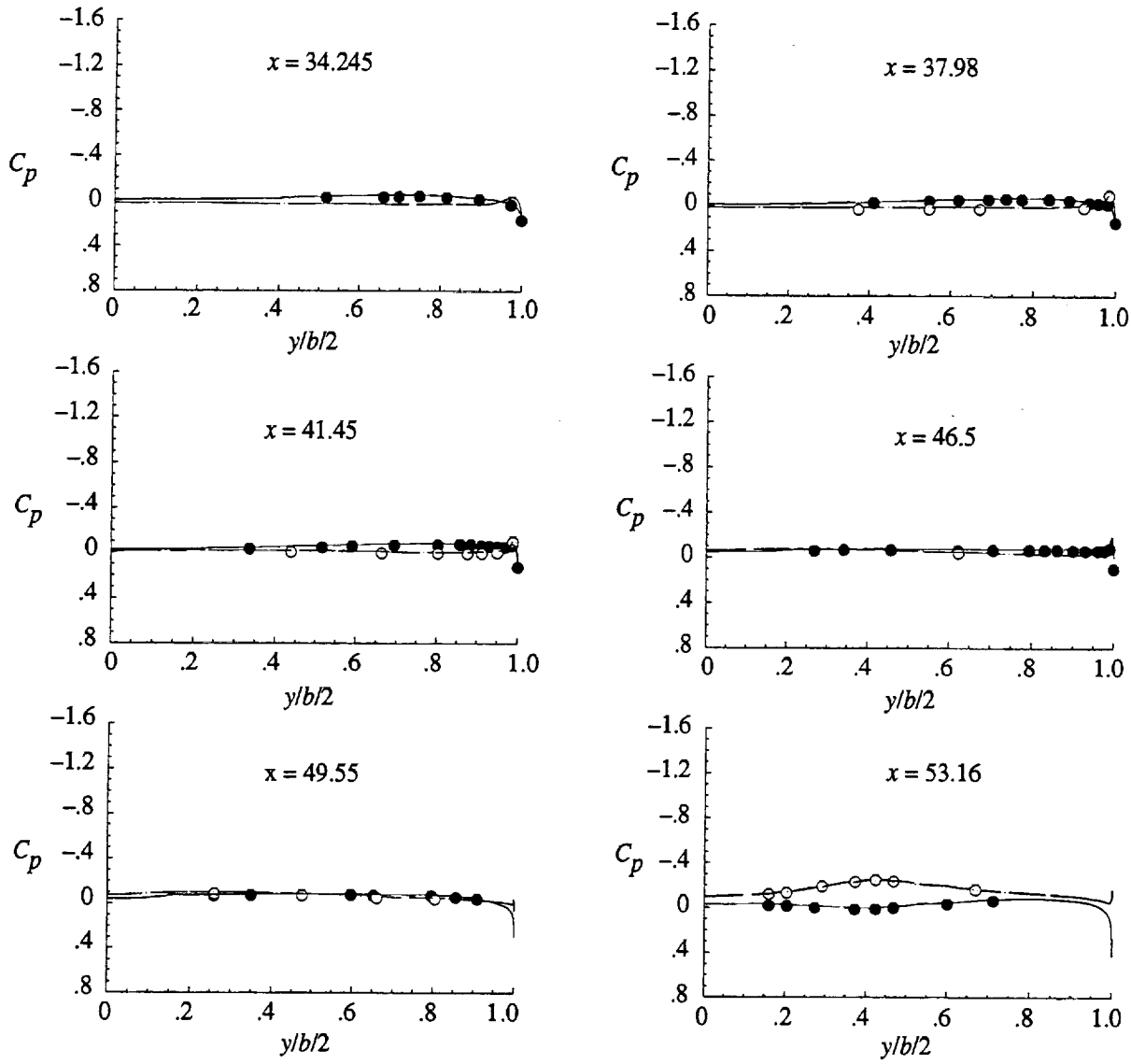

Figure 19. Spanwise wing pressure distributions. $M = 0.90$; $\alpha = 1.0°$; $Re_{\bar{c}} = 30 \times 10^6$. Dimensions are in inches.

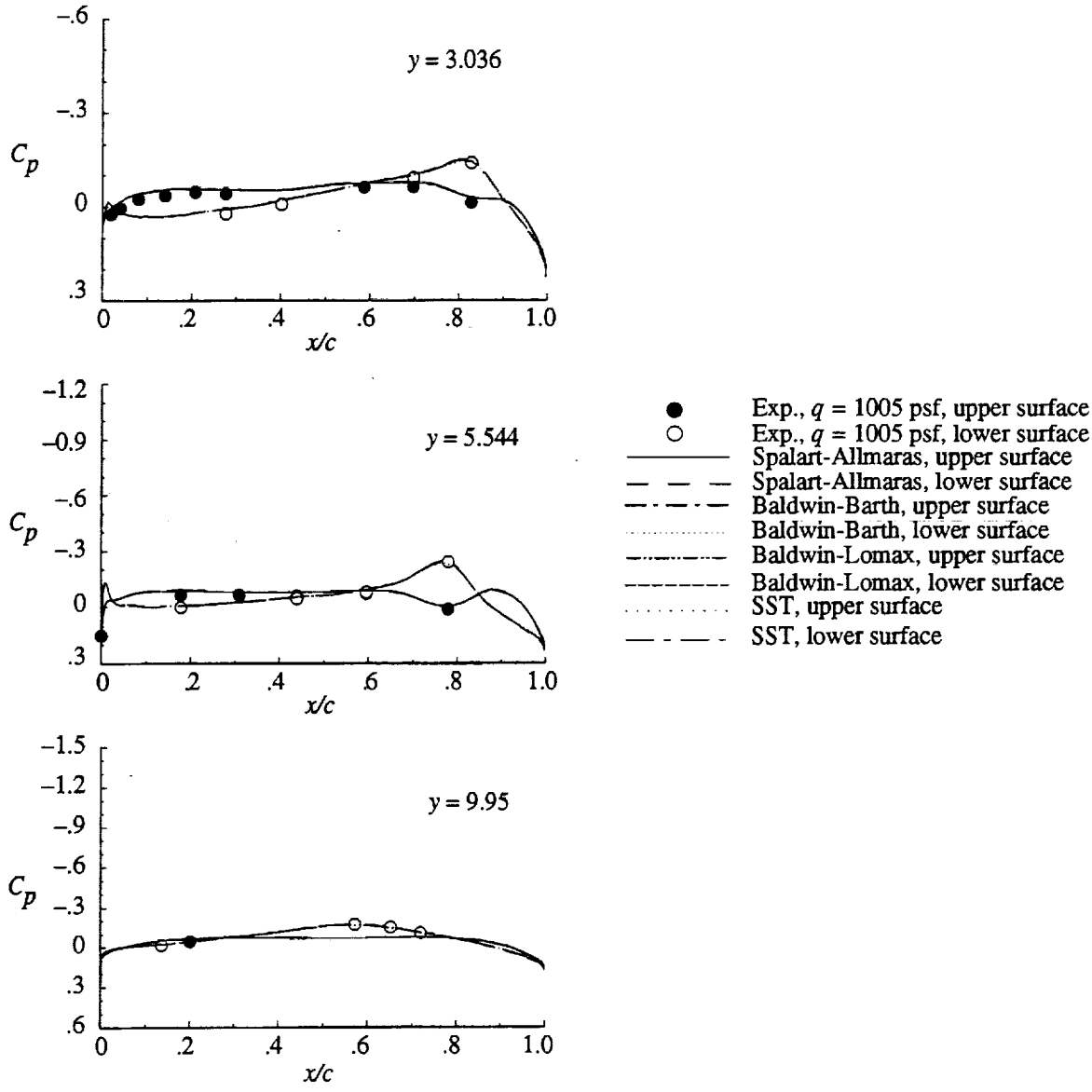

Figure 20. Chordwise wing pressure distributions. $M = 0.90$; $\alpha = 1.0°$; $Re_{\bar{c}} = 30 \times 10^6$. Dimensions are in inches.

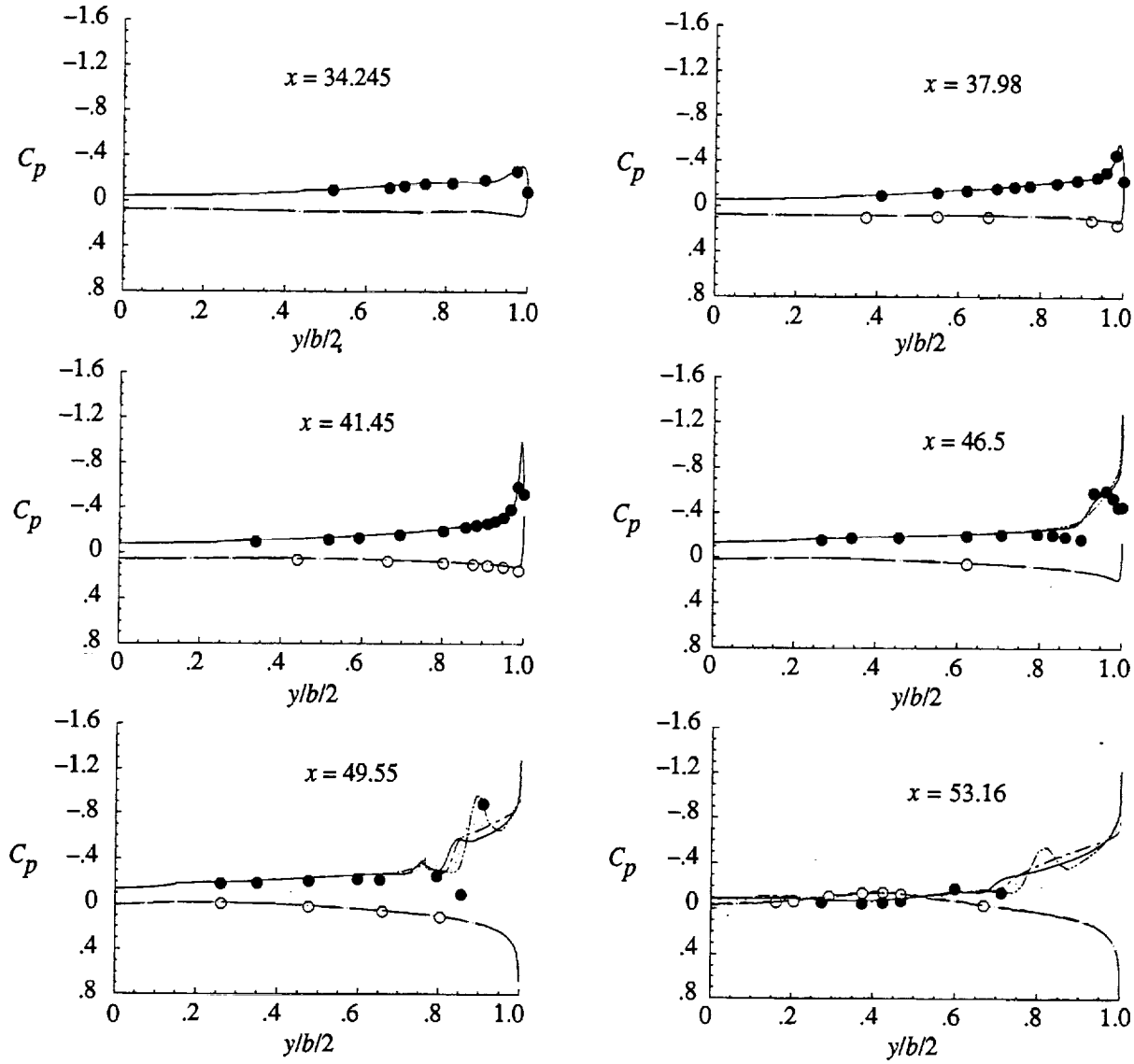

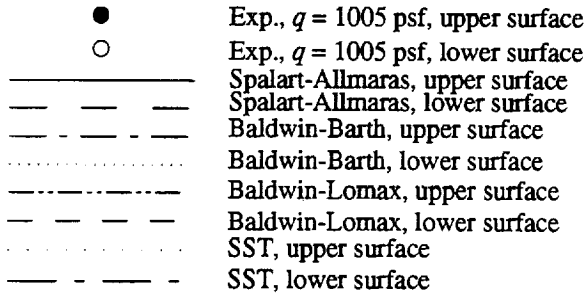

Figure 21. Spanwise wing pressure distributions. $M = 0.90$; $\alpha = 5.0°$; $Re_{\bar{c}} = 30 \times 10^6$. Dimensions are in inches.

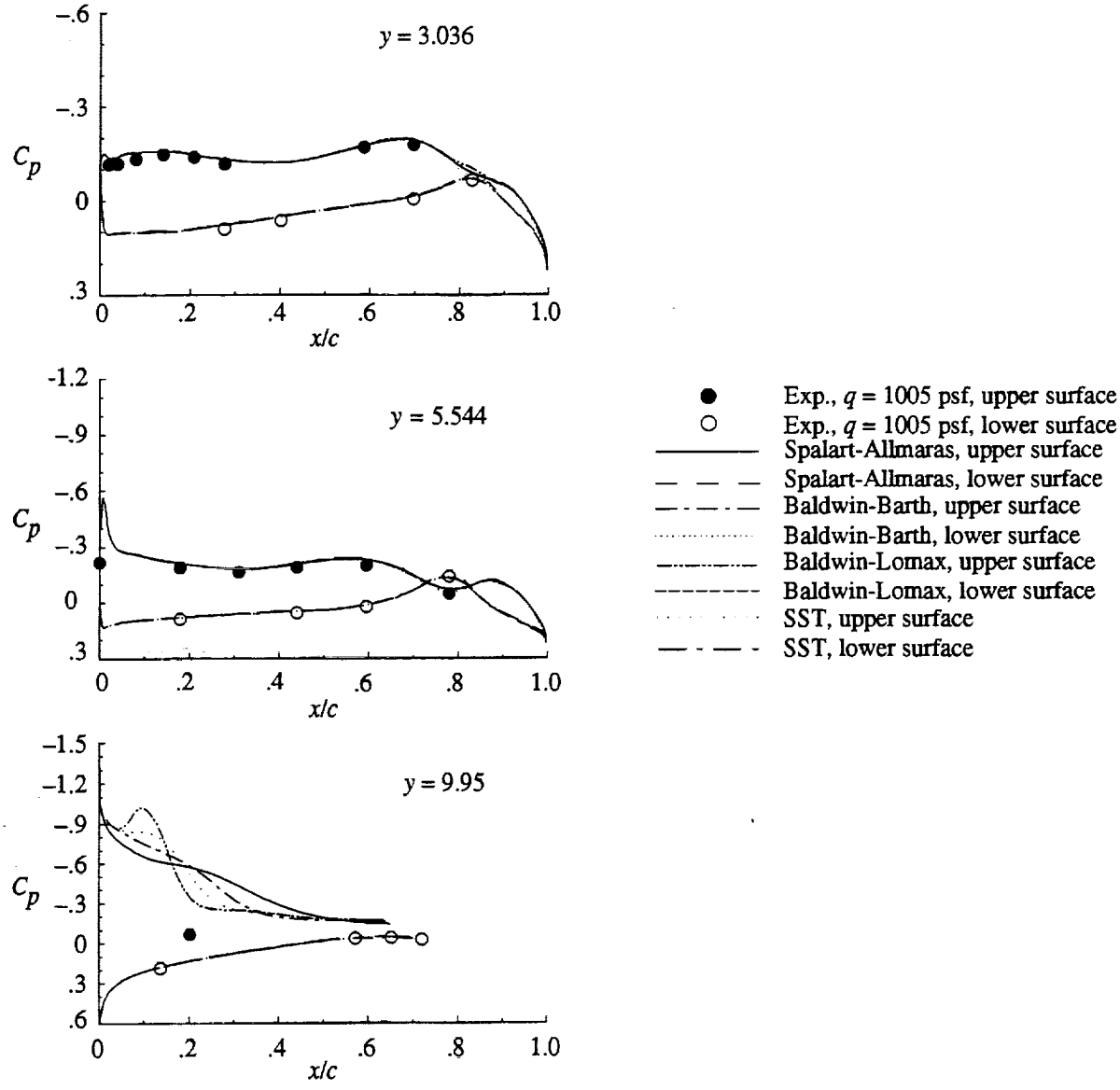

Figure 22. Chordwise wing pressure distributions. $M = 0.90$; $\alpha = 5.0°$; $Re_{\bar{c}} = 30 \times 10^6$. Dimensions are in inches.

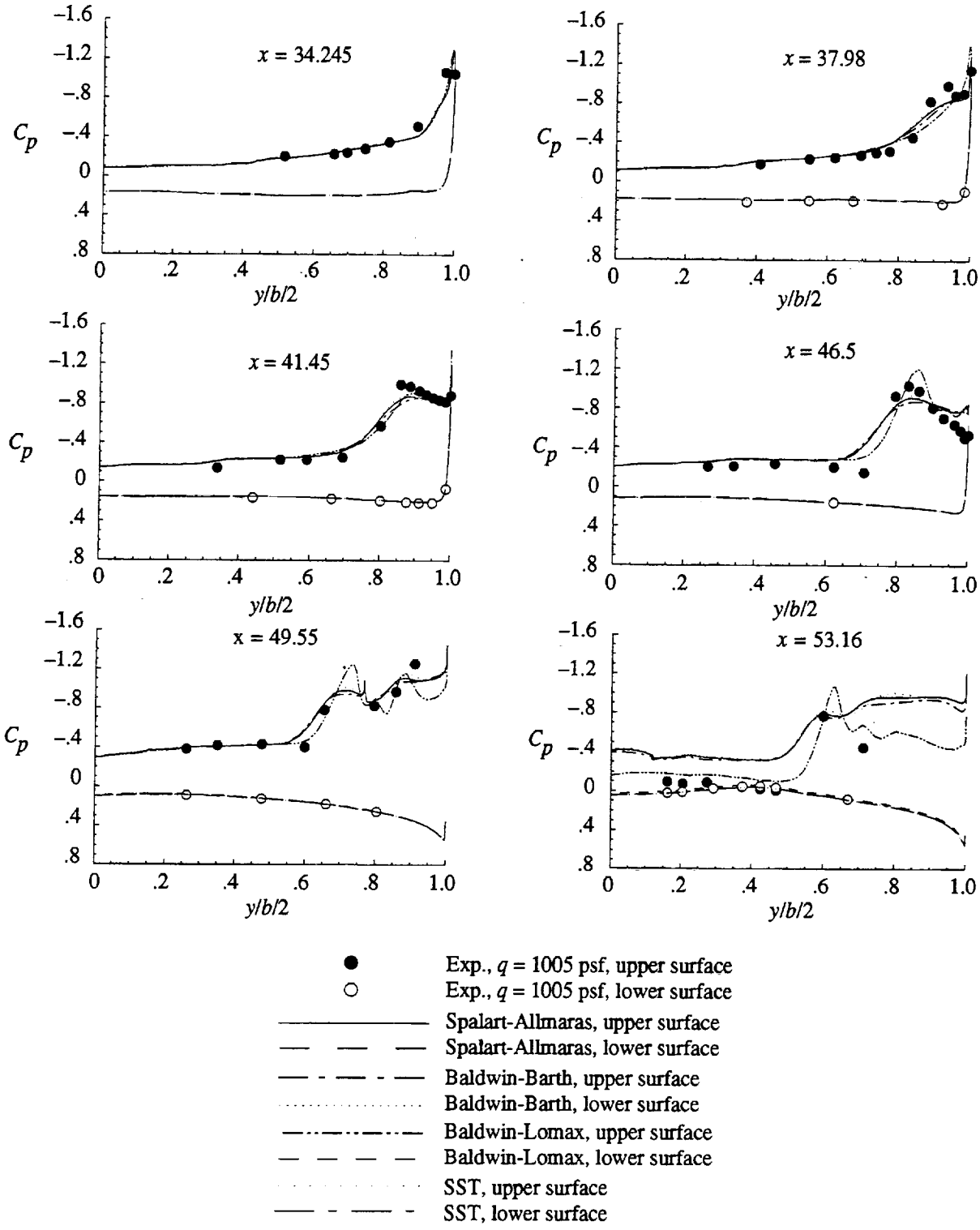

Figure 23. Spanwise wing pressure distributions. $M = 0.90$; $\alpha = 10.0°$; $Re_{\bar{c}} = 30 \times 10^6$. Dimensions are in inches.

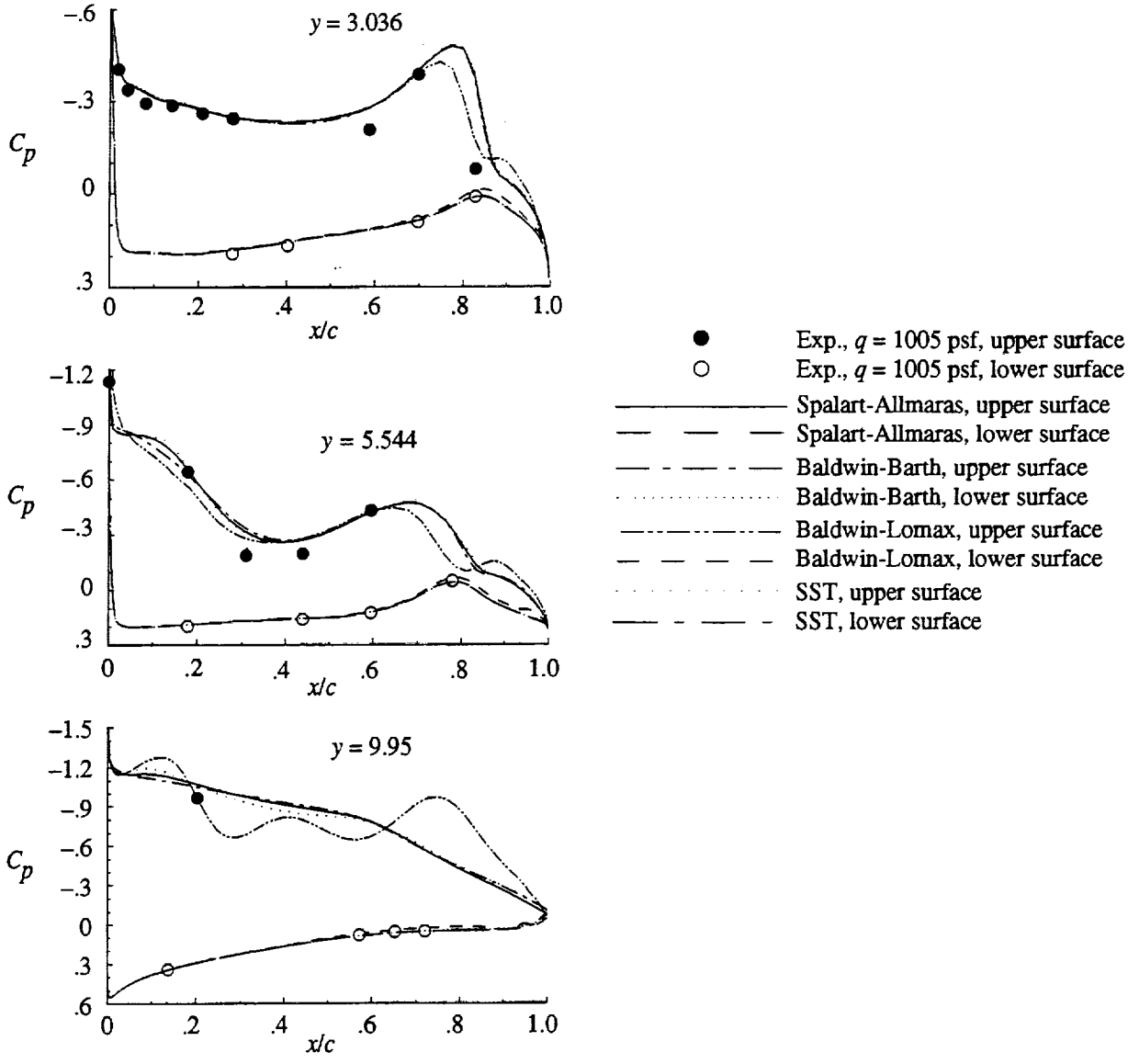

Figure 24. Chordwise wing pressure distributions. $M = 0.90$; $\alpha = 5.0°$; $Re_{\bar{c}} = 30 \times 10^6$. Dimensions are in inches.

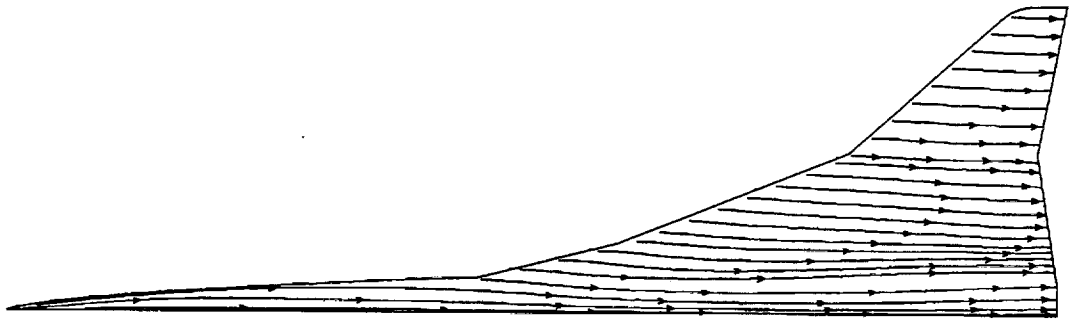

(a) Baldwin-Lomax.

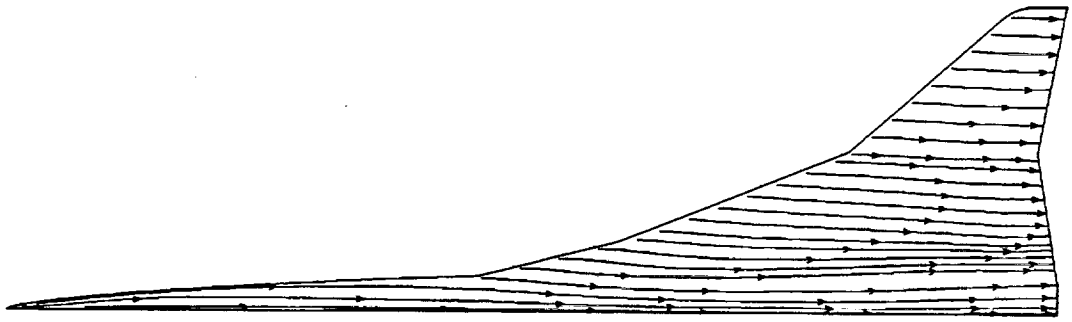

(b) Baldwin-Barth.

Figure 25. Computational surface streamlines. $M = 0.90$; $\alpha = 1.0°$; $\mathrm{Re}_{\bar{c}} = 30 \times 10^6$.

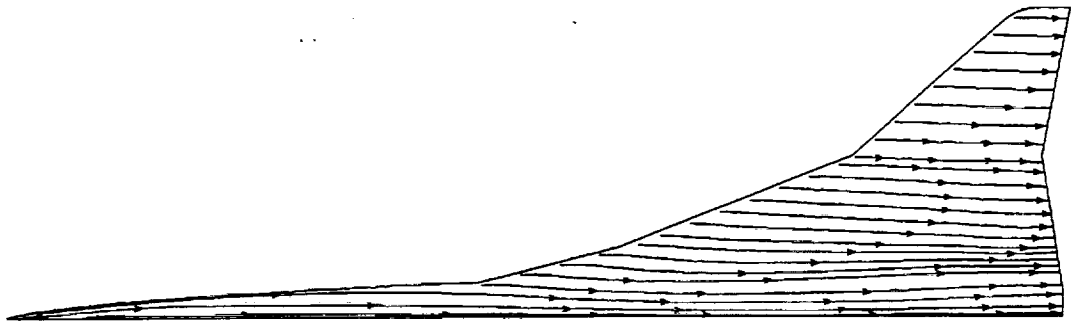

(c) Spalart-Allmaras.

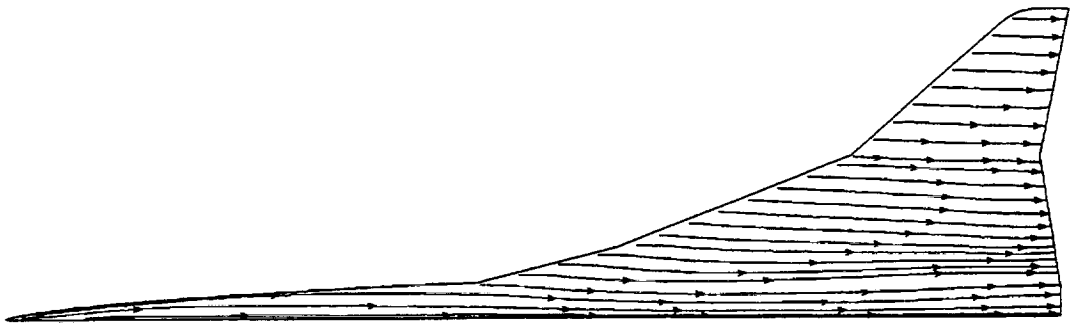

(d) SST.

Figure 25. Concluded.

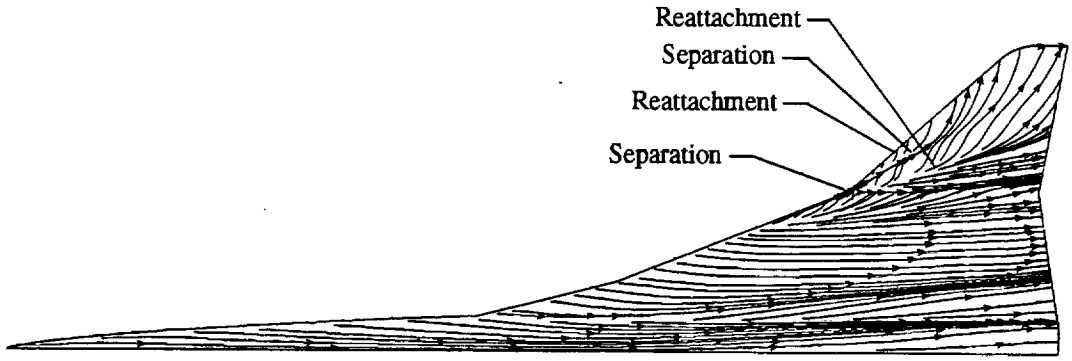

(a) Baldwin-Lomax.

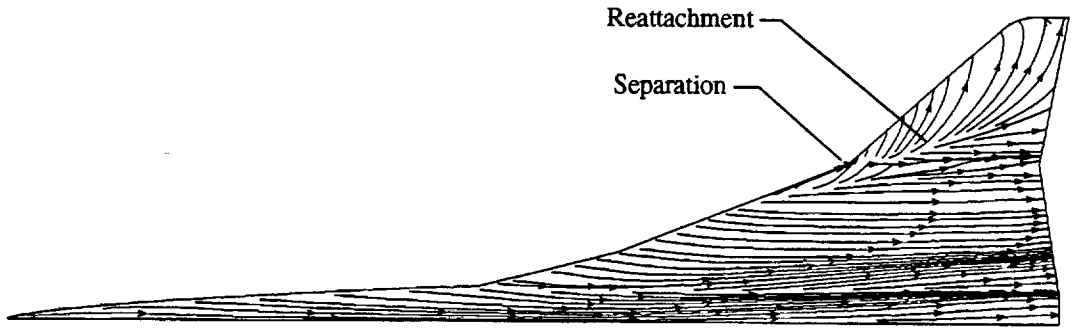

(b) Baldwin-Barth.

Figure 26. Computational surface streamlines. $M = 0.90$; $\alpha = 5.0°$; $\mathrm{Re}_{\bar{c}} = 30 \times 10^6$.

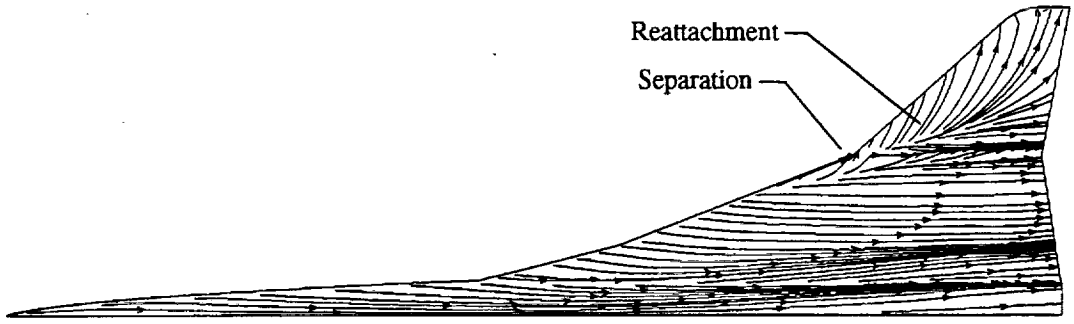

(c) Spalart-Allmaras.

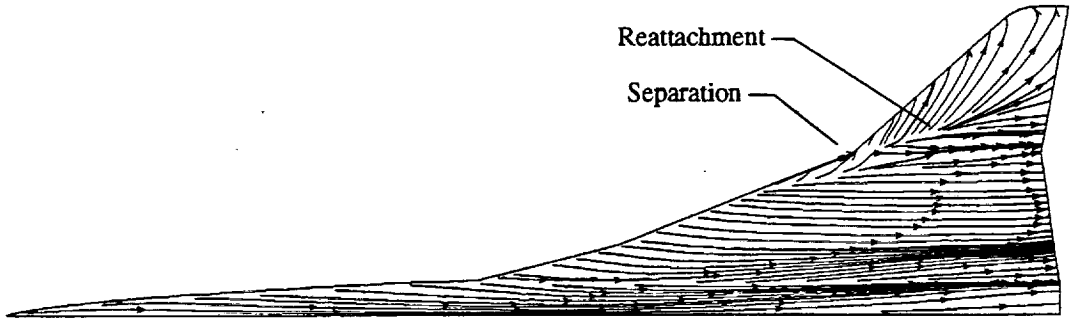

(d) SST.

Figure 26. Concluded.

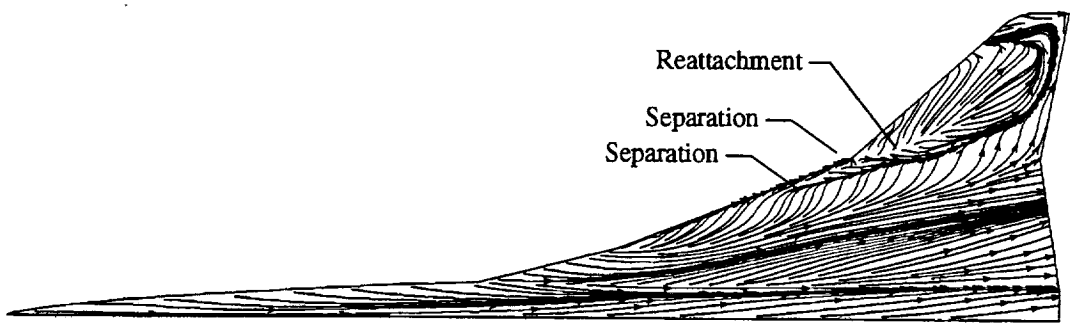

(a) Baldwin-Lomax.

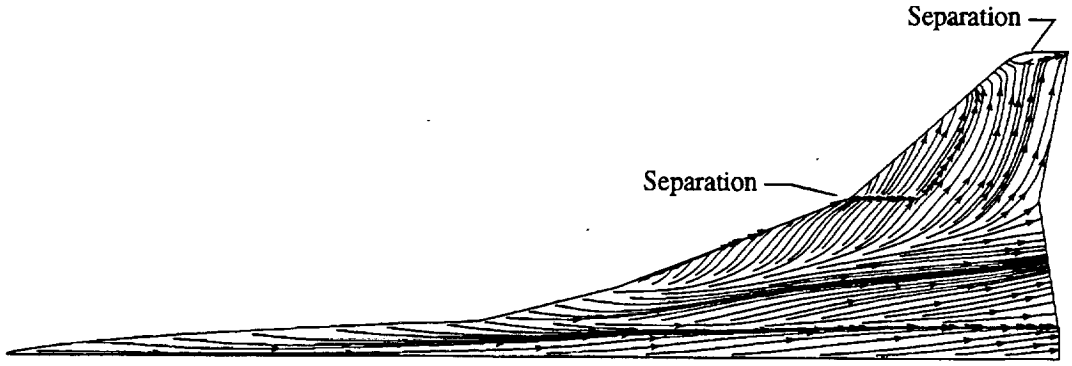

(b) Baldwin-Barth.

Figure 27. Computational surface streamlines. $M = 0.90$; $\alpha = 10.0°$; $\mathrm{Re}_{\bar{c}} = 30 \times 10^6$.

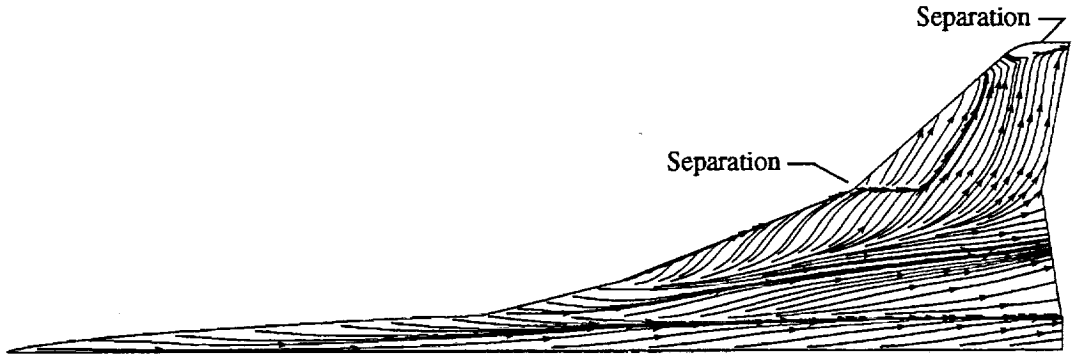

(c) Spalart-Allmaras.

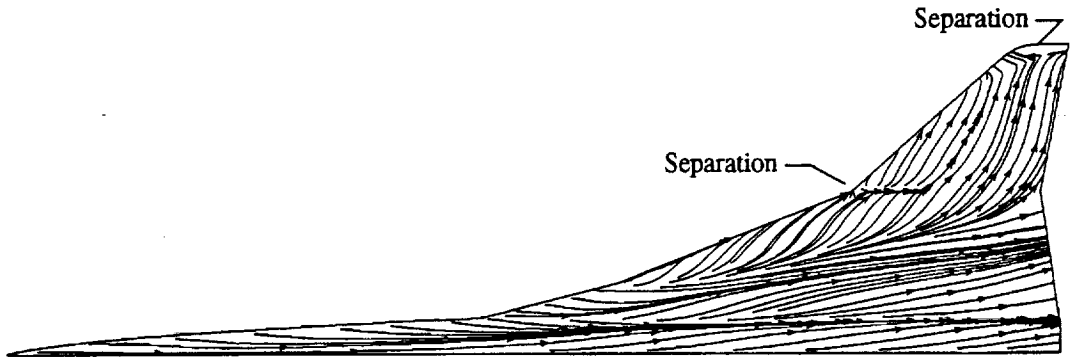

(d) SST.

Figure 27. Concluded.

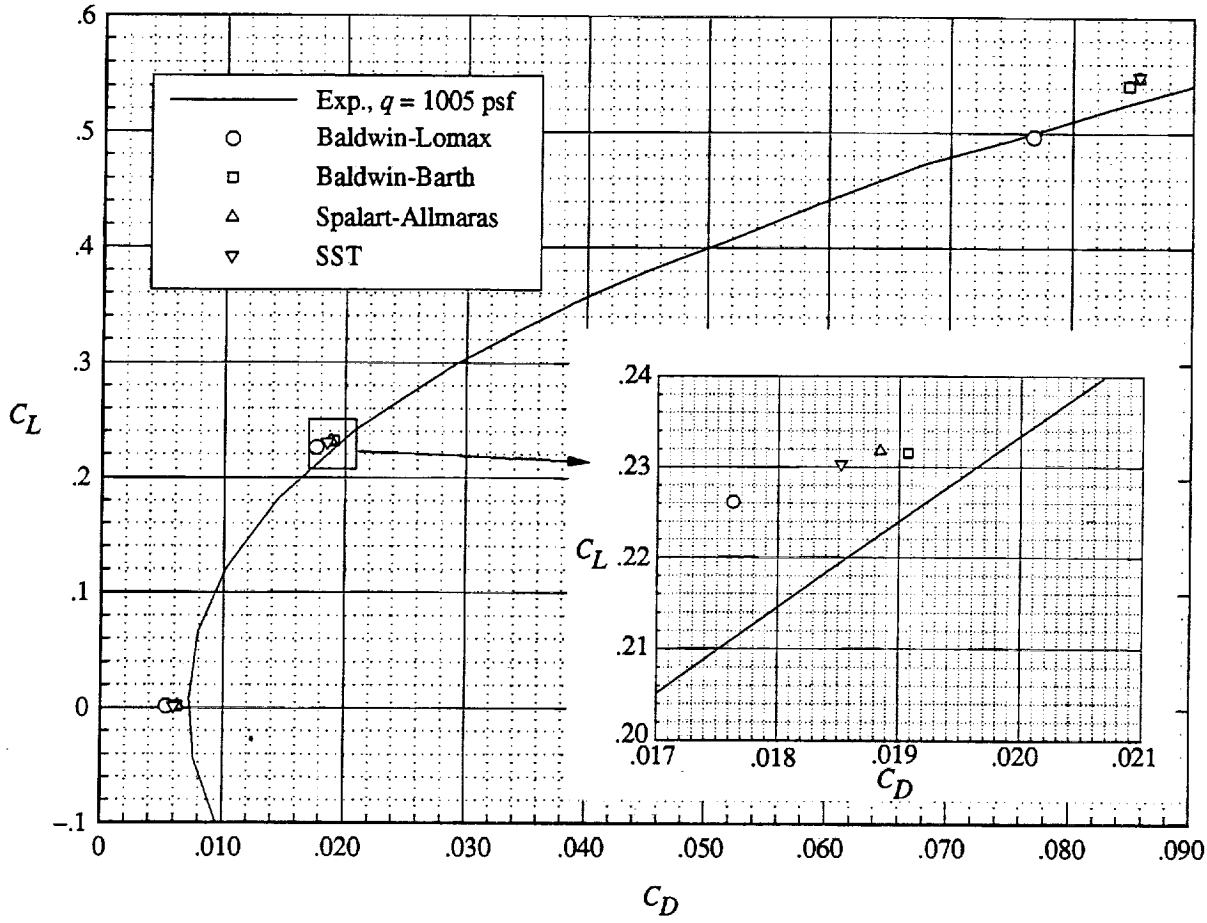

Figure 28. Drag polar. $M = 0.90$; $\mathrm{Re}_{\bar{c}} = 30 \times 10^6$.

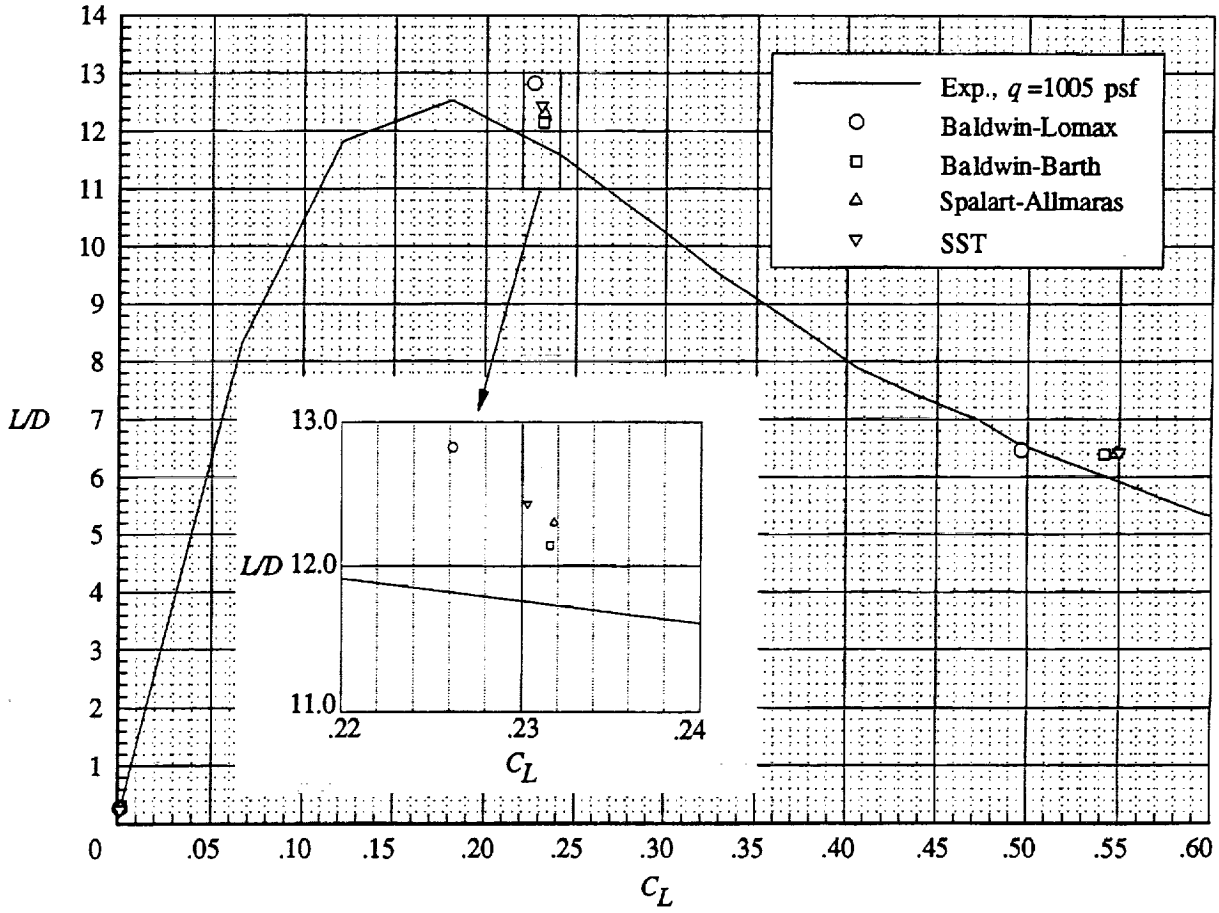

Figure 29. Lift-to-drag ratios. $M = 0.90$; $\mathrm{Re}_{\bar{c}} = 30 \times 10^6$.

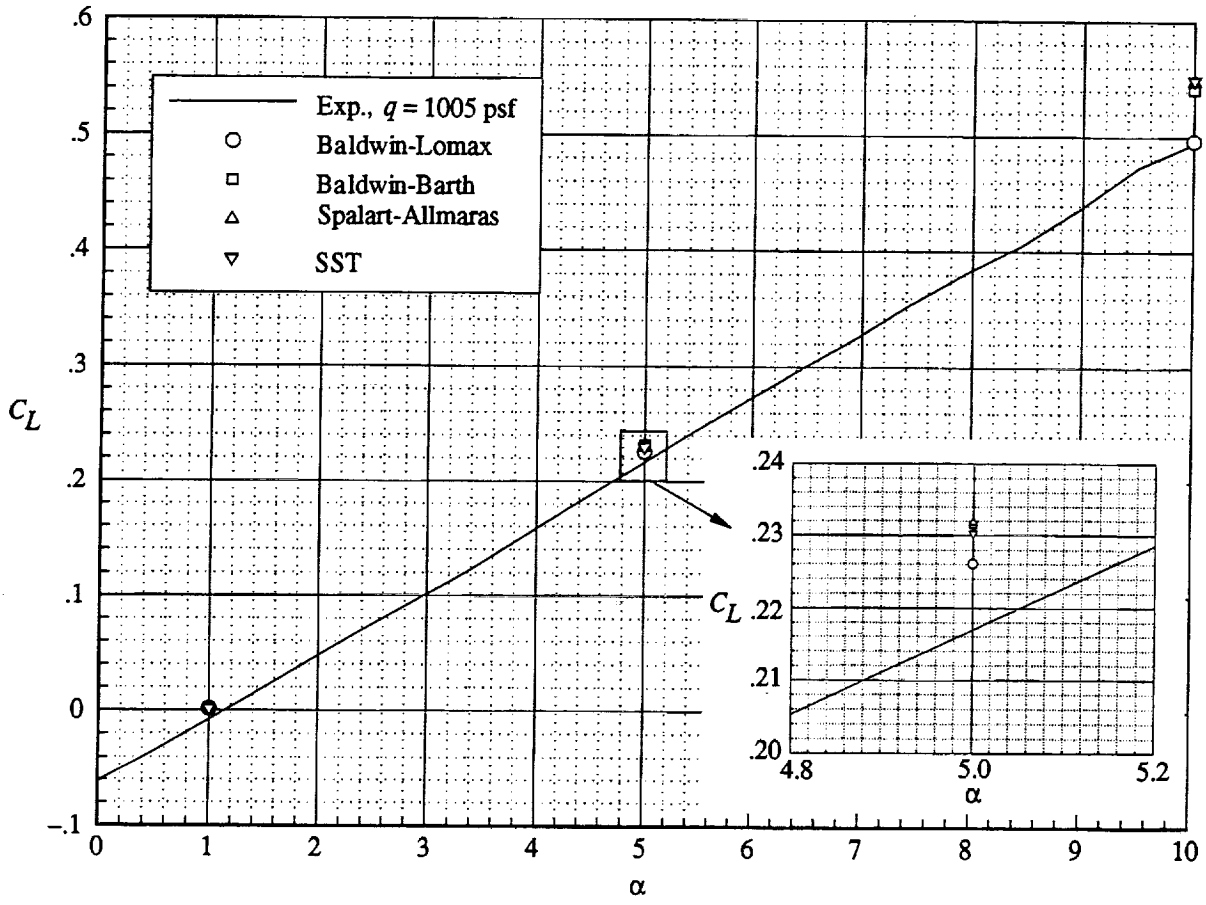

Figure 30. Lift curve. $M = 0.90$; $\mathrm{Re}_{\bar{c}} = 30 \times 10^6$.

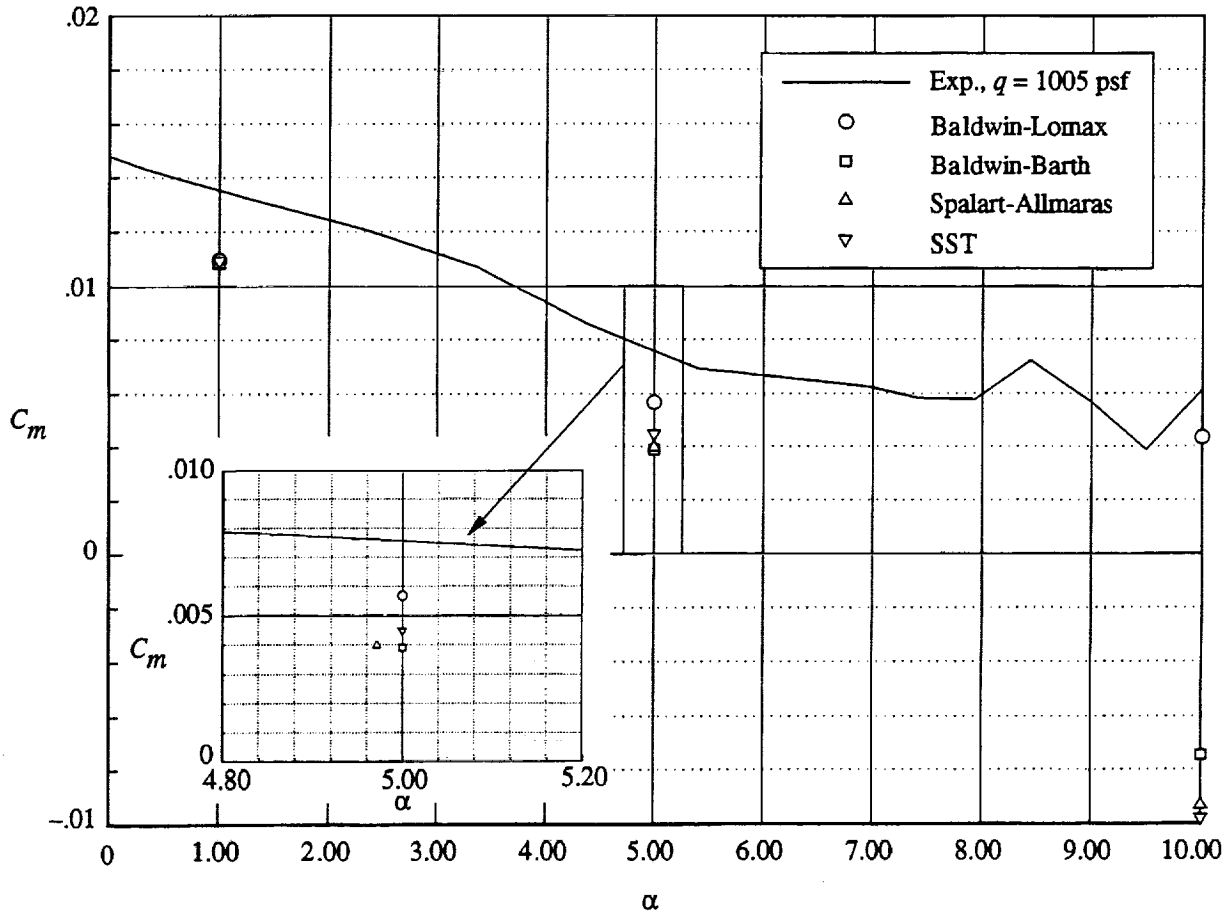

Figure 31. Pitching-moment curve. $M = 0.90$; $\mathrm{Re}_{\bar{c}} = 30 \times 10^6$.

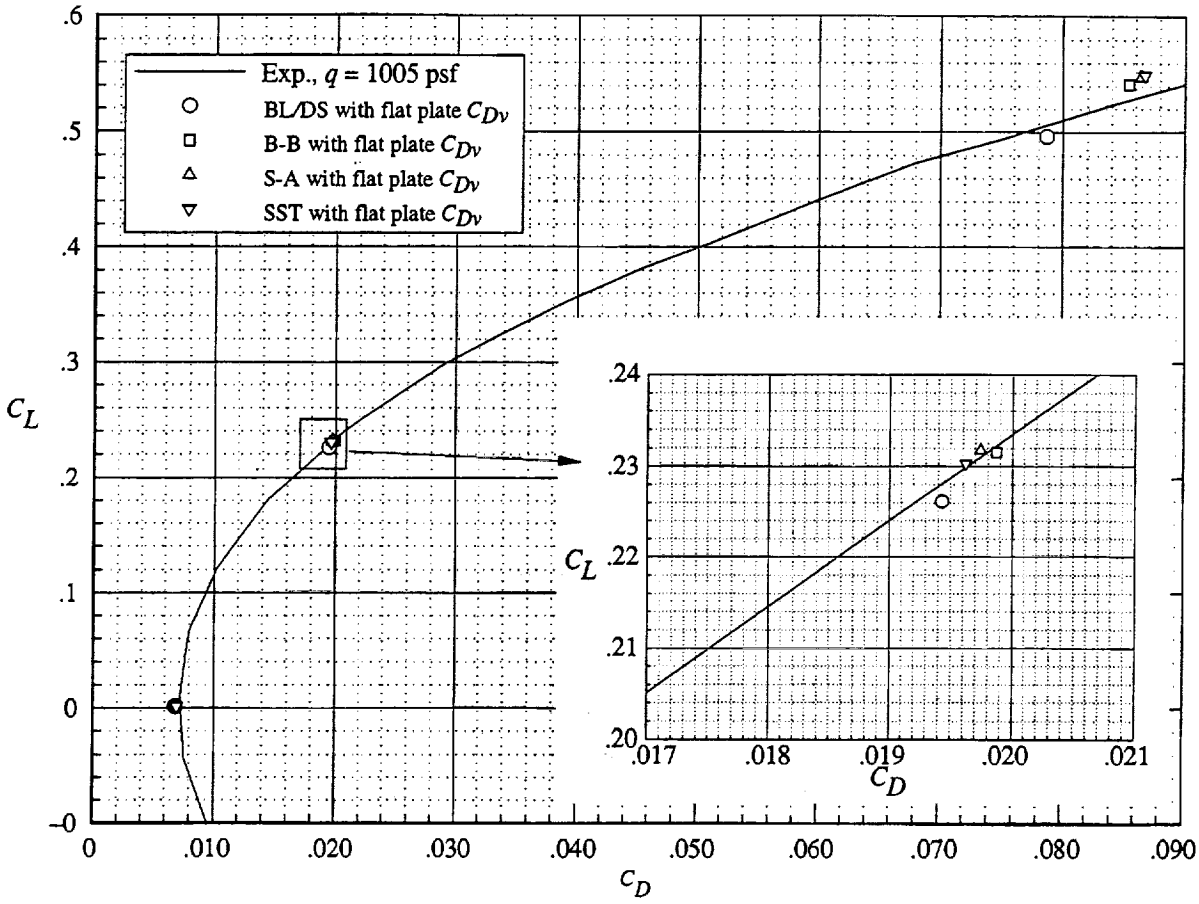

Figure 32. Drag polar using flat-plate equivalent viscous drag instead of computational viscous drag component. $M = 0.90$; $\mathrm{Re}_{\bar{c}} = 30 \times 10^6$.

REPORT DOCUMENTATION PAGE

Form Approved
OMB No. 0704-0188

1. AGENCY USE ONLY *(Leave blank)*	2. REPORT DATE	3. REPORT TYPE AND DATES COVERED
	December 1999	Technical Publication

4. TITLE AND SUBTITLE
Turbulence Model Comparisons for a High-Speed Aircraft

5. FUNDING NUMBERS
WU 537-07-20-24

6. AUTHOR(S)
Melissa B. Rivers and Richard A. Wahls

7. PERFORMING ORGANIZATION NAME(S) AND ADDRESS(ES)
NASA Langley Research Center
Hampton, VA 23681-2199

8. PERFORMING ORGANIZATION REPORT NUMBER
L-17597

9. SPONSORING/MONITORING AGENCY NAME(S) AND ADDRESS(ES)
National Aeronautics and Space Administration
Washington, DC 20546-0001

10. SPONSORING/MONITORING AGENCY REPORT NUMBER
NASA/TP-1999-209540

11. SUPPLEMENTARY NOTES

12a. DISTRIBUTION/AVAILABILITY STATEMENT
Unclassified–Unlimited
Subject Category 02 Distribution: Nonstandard
Availability: NASA CASI (301) 621-0390

12b. DISTRIBUTION CODE

13. ABSTRACT ***(Maximum 200 words)***

Four turbulence models are described and evaluated for transonic flows over the High-Speed Research/industry baseline configuration known as Reference H by using the thin-layer, upwind, Navier-Stokes solver known as CFL3D. The turbulence models studied are the equilibrium model of Baldwin-Lomax (B-L) with the Degani-Schiff (D-S) modifications, the one-equation Baldwin-Barth (B-B) model, the one-equation Spalart-Allmaras (S-A) model, and Menter's two-equation Shear Stress Transport (SST) model. The flow conditions, which correspond to tests performed in the National Transonic Facility (NTF) at Langley Research Center, are a Mach number of 0.90 and a Reynolds number of 30×10^6 based on mean aerodynamic chord for angles of attack of 1°, 5°, and 10°. The effects of grid topology and the representation of the actual wind tunnel model geometry are also investigated. Computed forces and surface pressures compare reasonably well with the experimental data for all four turbulence models.

14. SUBJECT TERMS	15. NUMBER OF PAGES
High-speed research	58
	16. PRICE CODE: A04

17. SECURITY CLASSIFICATION OF REPORT	18. SECURITY CLASSIFICATION OF THIS PAGE	19. SECURITY CLASSIFICATION OF ABSTRACT	20. LIMITATION OF ABSTRACT
Unclassified	Unclassified	Unclassified	UL

NSN 7540-01-280-5500

Standard Form 298 (Rev. 2-89)
Prescribed by ANSI Std. Z39-18
298-102